Chapter 9
Structure Determination of Membrane Peptides and Proteins by Solid-State NMR

Izuru Kawamura, Kazushi Norisada and Akira Naito

Abstract Solid-state nuclear magnetic resonance (NMR) spectroscopy provides useful information on the structure, topology, and orientation of peptides and proteins bound to lipid bilayers. The structure and orientation of membrane-associated peptides and proteins can be elucidated by analyzing structural constraints obtained from anisotropic chemical-shift interactions, nuclear dipolar interactions, or a combination of these interactions. Detailed structures of various peptides and proteins in their membrane-bound states can be studied by analyzing anisotropic chemical-shift interactions by, for example, chemical-shift oscillation analysis, and nuclear dipolar interactions using techniques such as polarity index slant angle wheel analysis. Magic-angle spinning (MAS) experiments coupled with cross-polarization (CP) and high-power decoupling (CP-MAS) techniques provide high-resolution ^{13}C and ^{15}N NMR signals for selectively or uniformly labeled membrane-bound peptides and proteins in solid-state NMR. Furthermore, homonuclear and heteronuclear dipolar interactions can be recoupled using various spin manipulation pulse sequences under MAS conditions. These experiments enable the correlation of ^{13}C–^{13}C and ^{13}C–^{15}N signals, allowing their assignment to specific amino acid residues and ultimately determination of the high-resolution structure of membrane-bound peptides and proteins.

Keywords Membrane peptide · Membrane protein · Chemical-shift interaction Nuclear dipolar interaction · Solid-state NMR

I. Kawamura (✉) · A. Naito
Faculty of Engineering, Yokohama National University,
79-5 Hodogayaku Tokiwadai, Yokohama 240-8501, Japan
e-mail: izuruk@ynu.ac.jp

A. Naito
e-mail: naito@ynu.ac.jp

K. Norisada
Graduate School of Engineering, Yokohama National University,
79-5 Hodogayaku Tokiwadai, Yokohama 240-8501, Japan
e-mail: k_norisada@iic.ihi.co.jp

The Nuclear Magnetic Resonance Society of Japan, *Experimental Approaches of NMR Spectroscopy*, https://doi.org/10.1007/978-981-10-5966-7_9

9.1 Introduction

Elucidation of both the structure and orientation of the membrane-bound structures of membrane-associated, biologically active peptides and proteins is important for full understanding of their biological functions and activities. These structures and orientations can be determined using structural and orientational constraints derived from magnetically anisotropic interactions, studied by solid-state NMR spectroscopy [1–6]. One such interaction is chemical-shift anisotropy (CSA), which typically appears as a dynamically averaged chemical-shift pattern. Using CSA interaction, the orientation of peptides and proteins in a lipid-bilayer environment can be derived [7]. Another interaction to be considered as a structural constraint is nuclear dipolar interaction between coupled nuclei. This type of interaction can be combined with chemical-shift constraints to provide detailed structural information regarding membrane-associated peptides and proteins [8]. Taken together, these constraints provide the dynamic structures, including detailed local structure, topology, and orientation of membrane-associated peptides and proteins [9]. However, complete structural information has only been determined for a limited number of these compounds.

Solid-state NMR analyses of biomolecules are typically performed using ^{13}C and ^{15}N nuclei, which exhibit spin-1/2. Solid-state NMR spectra yield enormously broadened signals, with line widths on the order of 20 kHz. Magic-angle spinning (MAS) experiments combined with cross-polarization (CP) and high-power decoupling (CP-MAS) provide high-resolution ^{13}C and ^{15}N NMR signals for selectively or uniformly labeled membrane-bound peptides and proteins. In solid-state NMR, homonuclear and heteronuclear dipolar interactions can be recoupled using various pulse sequences combined with multidimensional NMR techniques under MAS conditions. These experiments enable the correlation of ^{13}C and ^{15}N signals for assignment to amino acid residues and chemical shifts and distance constraints. These data can then be used to determine the high-resolution structure of membrane-associated peptides and proteins [10, 11].

In this review, we describe the experimental approaches used in solid-state NMR methods to determine the membrane-bound structures and orientations of antimicrobial peptides and membrane proteins.

9.2 Experimental Approaches Used in Solid-State NMR Spectroscopy

The broadened signals of spin-1/2 nuclei, including ^{13}C and ^{15}N, arise from nuclear interactions such as nuclear dipolar interactions and chemical-shift anisotropy (CSA), which are on the order of 20 kHz. A wealth of structural data in relation to interatomic distances and nuclear orientation to the applied magnetic field is contained in such broadened NMR signals in both the crystalline and non-crystalline

state and should be carefully analyzed in a site-specific manner using site-specific isotropic labeling. It is useful to orient the sample along the magnetic field, leading to relatively high-resolution signals. High-resolution signals can also be obtained by rotating the sample about an axis tilted by 54.7° to the magnetic field, called the magic angle. This high-resolution technique is combined with a recoupling technique to obtain further structural information on biologically significant molecules.

9.2.1 Experimental Details for Obtaining the Structures of Membrane-Associated Peptides and Proteins Using Anisotropic Interactions

9.2.1.1 Orientation Dependence of Chemical-Shift Interaction

The orientations of peptides bound to magnetically aligned lipid bilayers can be determined by analyzing the ^{13}C CSA of the carbonyl carbon in the peptide chain. Chemical-shift tensors for the carbonyl carbons can be clearly discerned from the spectral line shape, as shown in Fig. 9.1. When the peptide is completely rigid, 150 ppm of anisotropy will be observed in a low-temperature experiment (Fig. 9.1a, f). In contrast, when the temperature is increased above the liquid crystalline-to-gel phase-transition temperature (Tc), the molecules exhibit a large-amplitude rotational motion about the bilayer normal (Fig. 9.1A, C). In this case, an axially symmetric powder pattern is observed, as shown in Fig. 9.1b, g. Since bilayers tend to align with the magnetic field, narrow signals appear at either the $\delta_{//}$ or $\delta_{\perp}$ position when α-helical peptide molecules rotate about the bilayer parallel or bilayer normal (Fig. 9.1B(d), C(e), respectively). A slow MAS experiment can break down the alignment to exhibit an axially symmetric powder pattern (Fig. 9.1b, g). The molecule actually exhibits a reorientational motion about the bilayer normal (Fig. 9.1C) as evidenced by the axially symmetric pattern observed in dimyristoylphosphatidylglycerol (DMPG)–melittin bilayers (Fig. 9.1g) [7, 12].

When the rotor stops spinning, DMPG–melittin lipid-bilayer systems spontaneously orient with the magnetic field, and the membrane-bound molecules also align with the magnetic field. In most cases, membrane-bound biomolecules rotate about the membrane normal due to lateral diffusion of the lipid molecules in the liquid-crystalline phase (Fig. 9.1C). In the case of melittin, the entire molecule forms an α-helix in the membrane-bound state, and the helical axis rotates about the bilayer normal with tilt angle ζ and phase angle γ (Fig. 9.1A). In this case, the ^{13}C NMR signals of carbonyl carbons in the magnetically oriented lipid bilayer appear at the $\delta_{\perp}$ position (Fig. 9.1e, h) of the axially symmetric powder pattern (Fig. 9.1b, g). However, it must be stressed that the α-helix does not rotate about the helical axis.

The helical axis rotates rapidly about the bilayer normal, as shown in Fig. 9.1A, C; thus, Euler rotation matrices are used to transform the ^{13}C chemical-shift tensors from the principal-axis frame (PAF) to the helical molecular frame (HMF), then to

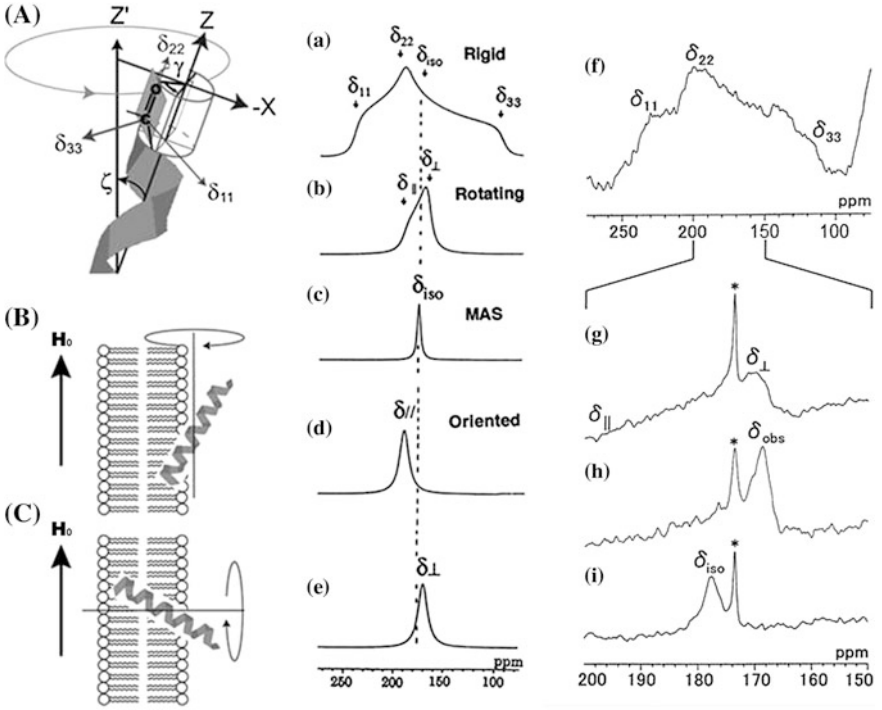

Fig. 9.1 **A** Direction of the principal axis of the ^{13}C chemical-shift tensor of the C=O group. **B** The helical axis rotates about the magnetic field (H_0). **C** The helical axis rotates about the bilayer normal. ^{13}C-NMR spectral patterns of the C=O carbons corresponding to the orientation of the α-helix with respect to the surface of the magnetically oriented lipid bilayers. Simulated spectra were calculated using $\delta_{11} = 241$, $\delta_{22} = 189$, and $\delta_{33} = 96$ ppm for the rigid case (*a*), rotation about the unique axis without orienting to the magnetic field (slow MAS condition) (*b*), MAS (*c*), rotation about the magnetic field (*d*), and rotation about the bilayer normal (*e*). ^{13}C NMR of [1-^{13}C]Ile4-melittin–DMPG bilayer system in the rigid state at −60 °C (*f*), in the slow MAS condition at 40 °C (*g*), in the oriented condition at 40 °C (*h*), and in the fast MAS condition at 40 °C (*i*) [4]

the molecular rotating frame (MRF), and finally to the laboratory frame (LF), using a three-step transformation (Fig. 9.2) to analyze the dynamic structures of melittin bound to membranes. Assuming that the δ_{zz}-axis for the carbonyl carbon is parallel to the helical axis (the *Z*-axis) of melittin (Fig. 9.2a) for a transformation from the PAF (δ_{11}, δ_{22}, δ_{33}) to the HMF (*X*, *Y*, *Z*), the matrix R_1 for the Euler rotation is given by:

$$R_1(\alpha', \beta', \gamma') = R_1\left(\frac{\pi}{2}, \frac{\pi}{2}, \gamma - \frac{\pi}{2}\right) = \begin{bmatrix} \cos\gamma & 0 & -\sin\gamma \\ -\sin\gamma & 0 & -\cos\gamma \\ 0 & 1 & 0 \end{bmatrix}, \qquad (9.1)$$

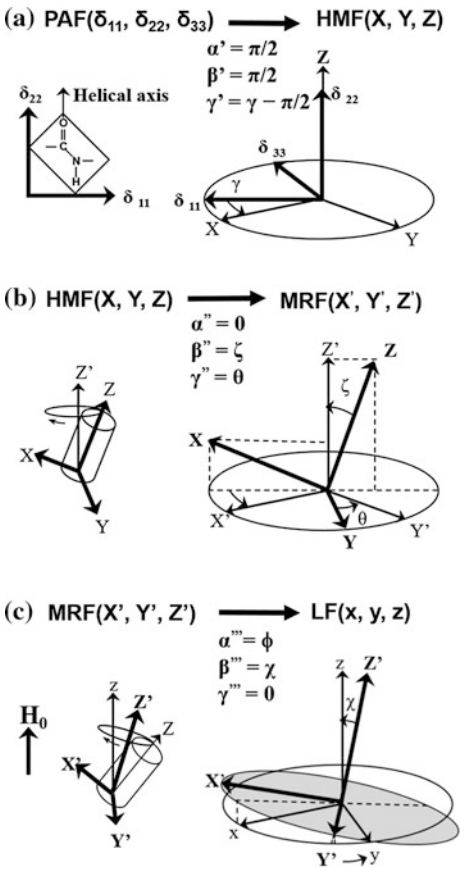

Fig. 9.2 Coordinate conversion using Euler rotation angles for description of the rotational motion of α-helical melittin bound to the membrane. **a** Rotation from the principal-axis frame (*PAF*) to the helical molecular frame (*HMF*). **b** Rotation from the HMF to the molecular rotation frame (*MRF*). **c** Rotation from the MRF to the laboratory frame (*LF*)

where γ is a constant and the helical axis is directed from the N- to the C-terminus. When the helical axis rotates about the Z'-axis at a constant tilt angle of ζ to the helical axis (Fig. 9.2b) for a transformation from the HMF to the MRF(X', Y', Z'), the matrix R_2 for the Euler rotation is given by:

$$R_2(\alpha'', \beta'', \gamma'') = R_2(0, \zeta, \theta) = \begin{bmatrix} \cos\zeta\cos\theta & \sin\theta & -\sin\zeta\cos\theta \\ -\cos\zeta\sin\theta & \cos\theta & \sin\zeta\sin\theta \\ \sin\zeta & 0 & \cos\zeta \end{bmatrix}, \quad (9.2)$$

where θ varies continuously with rotational motion at the Z'-axis. It is emphasized that the direction of the tilt angle is important for determining the interhelical angle for molecules containing more than two helices. If the rotation axis inclines χ to the magnetic field (the z-axis) (Fig. 9.2c) for transformation from the MRF to the LF(x, y, z), the matrix R_3 of the Euler rotation is given by:

$$R_3(\alpha''', \beta''', \gamma''') = R_3(\Phi, \chi, 0) = R_3\left(\frac{\pi}{2}, \chi, 0\right) = \begin{bmatrix} 0 & \cos\chi & -\sin\chi \\ -1 & 0 & 0 \\ 0 & \sin\chi & \cos\chi \end{bmatrix} \tag{9.3}$$

Here, ϕ is an arbitrary constant under the static condition and $\phi = \pi/2$ is chosen. Consequently, a rotation matrix of $R = R_3R_2R_1$ transforms the chemical-shift tensor from the PAF to the LF, as:

$$\tilde{\delta}^{\mathrm{LF}} = R \cdot \tilde{\delta}^{\mathrm{PAF}} \cdot R^{-1} \tag{9.4}$$

When the rotation axis inclines 90° to the magnetic field, the observed chemical-shift value $(\delta_{zz})_{\chi=\pi/2} = \delta_{\perp}$ is expressed as

$$\begin{aligned}\delta_{\perp} = {} & \sin^2\theta\left[\cos^2\zeta\left(\delta_{11}\cos^2\gamma + \delta_{33}\sin^2\gamma - \delta_{22}\right) - \left(\delta_{11}\sin^2\gamma + \delta_{33}\cos^2\gamma - \delta_{22}\right)\right] \\ & + \frac{1}{2}\sin 2\theta\cos\zeta\sin 2\gamma(\delta_{11} - \delta_{33}) + \delta_{11}\sin^2\gamma + \delta_{33}\cos^2\gamma\end{aligned} \tag{9.5}$$

On the other hand, when the rotation axis inclines 0° to the magnetic field, the observed chemical-shift value $(\delta_{zz})_{\chi=0} = \delta_{//}$ is expressed as

$$\delta_{\parallel} = -\cos^2\zeta\left(\delta_{11}\cos^2\gamma + \delta_{33}\sin^2\gamma - \delta_{22}\right) + \left(\delta_{11}\cos^2\gamma + \delta_{33}\sin^2\gamma\right) \tag{9.6}$$

The chemical-shift anisotropy, $\Delta\delta = \delta_{//} - \delta_{\perp}$, is obtained by combining Eqs. (9.5) and (9.6) as

$$\begin{aligned}\Delta\delta = {} & \left[\left(\delta_{11}\cos^2\gamma + \delta_{33}\sin^2\gamma\right) - \cos^2\zeta\left(\delta_{11}\cos^2\gamma + \delta_{33}\sin^2\gamma - \delta_{22}\right)\right] \\ & - \sin^2\theta\left[\cos^2\zeta\left(\delta_{11}\cos^2\gamma + \delta_{33}\sin^2\gamma - \delta_{22}\right) - \left(\delta_{11}\sin^2\gamma + \delta_{33}\cos^2 - \delta_{22}\right)\right] \\ & - \frac{1}{2}\sin 2\theta\cos\zeta\sin 2\gamma(\delta_{11} - \delta_{33}) - \delta_{11}\sin^2\gamma - \delta_{33}\cos^2\gamma\end{aligned} \tag{9.7}$$

Here, functions of θ can be averaged over a cycle when the helical axis rotates rapidly about the axis parallel to the membrane normal that corresponds to the Z'-axis. In this case, we obtain an expression where the averaged anisotropy depends on the phase angle, γ, of the peptide plane about the helical axis, and the tilt angle, ζ, of the helical axis from the rotation axis as

$$\overline{\Delta\delta} = \frac{3}{2}\sin^2\zeta\left(\delta_{11}\cos^2\gamma + \delta_{33}\sin^2\gamma - \delta_{22}\right) + \left(\delta_{22} - \frac{\delta_{11} + \delta_{33}}{2}\right) \tag{9.8}$$

Since the C- and N-terminal regions of melittin adopt α-helical structures, the phase angle, γ, varies by −100° per consecutive residue in the direction toward the

C-terminus. Equation (9.8) indicates that the oscillations of $\overline{\Delta\delta}$ of the each carbonyl carbon can be changed as a function of γ along the consecutive amino acid sequence in the α-helical region. The amplitude of the oscillation depends on the tilt angle ζ. We call this behavior as chemical-shift oscillation.

When an α-helical peptide has a large tilt angle ζ, the $\Delta\delta$ value exhibits a large amplitude, as shown in Fig. 9.3. Using this property of $\Delta\delta$, the tilt angle ζ of the α-helical axis can be determined with respect to the bilayer normal by analyzing the anisotropic ^{13}C chemical-shift values of the carbonyl carbon of consecutive amino acid residues in the α-helical region (Fig. 9.3a). When a peptide forms an ideal α-helical structure, it can be assumed that the interpeptide plane angle for consecutive peptide planes is 100°. This tilt angle can be accurately obtained by analyzing the root-mean-square deviation (RMSD) for the observed and calculated CSAs using Eq. (9.9).

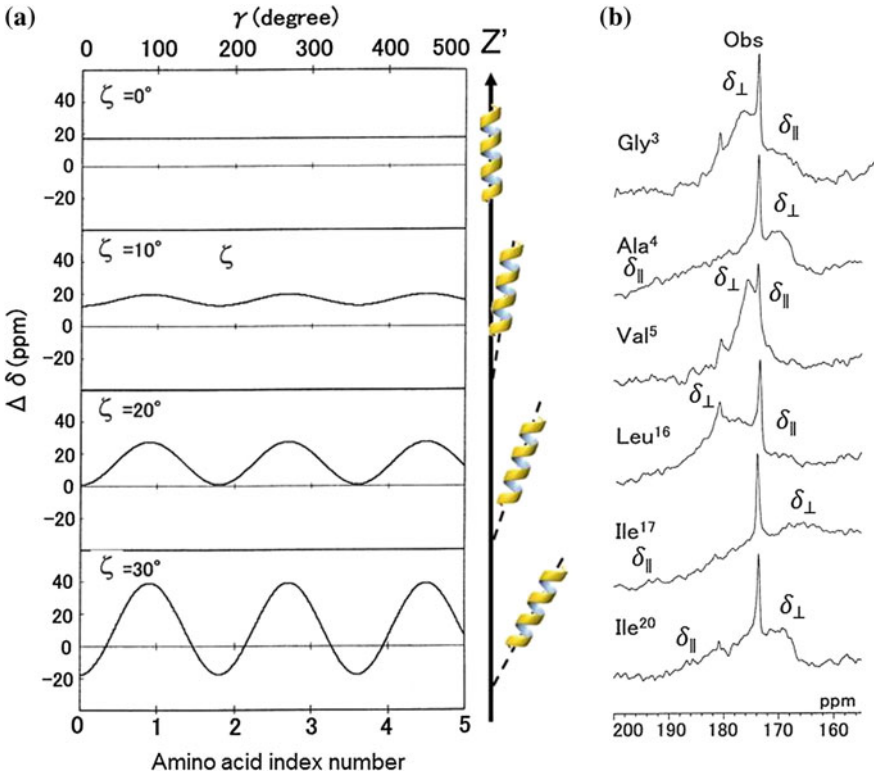

Fig. 9.3 **a** Chemical-shift oscillation curves of chemical-shift anisotropy, $\Delta\delta = \delta_{//}\text{-}\delta_{\perp}$, against the phase angle, γ, of the peptide plane for the amino acid residues as a function of the tilt angles, ζ, of the α-helical axis relative to the bilayer normal (Z'-axis) [4]. **b** ^{13}C chemical-shift powder patterns of [1-^{13}C]Gly3-, [1-^{13}C]Ala4-, [1-^{13}C]Val5, [1-^{13}C]Leu16, [1-^{13}C]Ile17, and [1-^{13}C] Ile20-melittin–DMPG bilayer system at 40 °C [54]

$$\mathrm{RMSD} = \left[\sum_{i}^{N} \{(\Delta\delta_{\mathrm{obs}})_i - (\Delta\delta_{\mathrm{calc}}))_i\}\}^2/N\right]^{1/2} \tag{9.9}$$

where $(\Delta\delta_{\mathrm{obs}})_i$ is the experimentally obtained chemical-shift anisotropy of the ith amino acid residue and $(\Delta\delta_{\mathrm{calc}})_i$ is the calculated chemical-shift anisotropy of the ith amino acid residues using the observed δ_{11}, δ_{22}, and δ_{33} values for the ith amino acid residue. N is the number of amino acid residues to be considered.

It is stressed that in chemical-shift oscillation analysis, lipid bilayers are not necessarily aligned with the magnetic field.

9.2.1.2 Orientation Dependence of Nuclear Dipolar Interactions

Similar information can be obtained by observing ^{15}N–^{1}H dipolar interactions in the peptide backbone. Polarization inversion spin exchange at the magic angle (PISEMA), a type of separated local-field 2D NMR spectroscopy, provides excellent resolution in the dipolar dimension in the correlation spectra between ^{15}N chemical-shift values and ^{15}N–^{1}H dipolar interaction [13, 14]. PISEMA was developed based on the flip-flop Lee-Goldberg phase- and frequency-switched pulse sequence, which is used to spin-lock ^{1}H spins along the magic angle to suppress homonuclear dipolar interactions. Sample heating is a serious problem in PISEMA, particularly when analyzing hydrated samples containing membrane proteins. This problem can be overcome by drastically reducing the radio frequency (rf) field [15, 16] or using a resonance coil designed for minimizing sample heating [17]. Offset problems encountered in PISEMA are overcome using the broadband PISEMA technique [18].

A characteristic circular pattern wheel, known as a polarity index slant angle (PISA), is observed in PISEMA (^{15}N chemical shifts, ^{1}H–^{15}N dipolar interaction correlation) 2D NMR spectra when an α-helix is formed in the membrane. The shape of the wheel is sensitive to the tilt angle of the α-helix with respect to the bilayer normal [19–21] (Fig. 9.4). By examining the PISA wheel, one can evaluate the amino acid residues involved in the α-helix, even if the amino acid sequence is not known. When the helical axis is parallel to the bilayer normal, all of the amino sites have an identical orientation relative to the direction of the applied magnetic field, and therefore, all of the resonances overlap with the same ^{1}H–^{15}N dipolar couplings and ^{15}N chemical-shift frequencies. Tilting the helix away from the membrane normal breaks the symmetry, introducing variation in the orientations of the amide N–H bond vectors relative to the field direction. This is manifested in the spectra as dispersions of both the ^{1}H–^{15}N dipolar couplings and the ^{15}N chemical-shift frequencies, as shown in Fig. 9.4b. Thus, the tilt angle of the helical axis can be accurately determined.

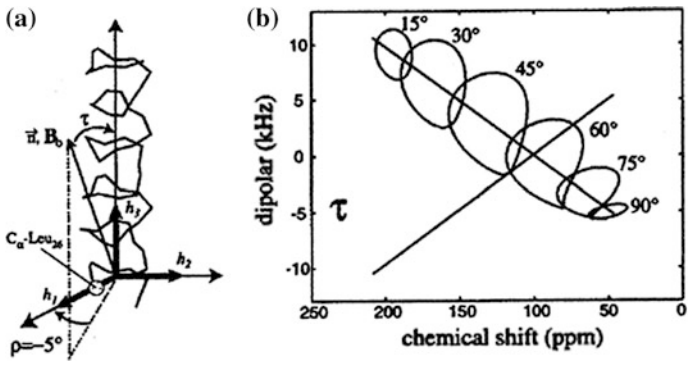

Fig. 9.4 The generation of "PISA wheels." **a** Definitions of τ and ρ for an α-helix. $\tau = 0°$ occurs when the helix axis, h_3, is parallel to B_0. $\rho = 0°$ occurs when the projection of B_0 onto a plane perpendicular to, h_3, makes an angle of 0° with h_1, the radial axis of the helix that passes through the Cα carbon of Leu26 of the M2-TMP helix [22]. **b** *Circles* drawn for one of the dipolar transitions using average values for the ^{15}N chemical-shift tensor elements ($\sigma_{11} = 31.3$, $\sigma_{22} = 55.2$, $\sigma_{33} = 201.8$ ppm) and the relative orientations of the ^{15}N–^{1}H dipolar and ^{15}N chemical-shift tensor, given by $\theta = 17°$, the angle of the peptide plane between σ_{22} and v (parallel to the N–H bond). Note that the center of the PISA wheel falls on a line that passes through the ^{15}N isotropic chemical shift (96 ppm) at 0 kHz on the dipolar scale [22]

9.2.1.3 Interatomic Distance Measurements by REDOR

Solid-state NMR allows quite accurate determination of internuclear distances by looking at the recoupled dipolar interaction, thereby providing extensive information on the three-dimensional (3D) structures of biomolecules. The rotational echo double resonance (REDOR) [23] technique recouples the relatively weak heteronuclear dipolar interaction under the MAS condition by applying a π pulse synchronous with the rotor period. Consequently, the transverse magnetization cannot be refocused completely at the end of the rotor cycle, leading to a reduction of the echo amplitude. The extent of the reduction of the echo amplitude as a function of the number of rotor periods depends on the strength of the heteronuclear dipolar interaction. This method is extensively used to determine relatively remote interaction distances on the order of 2–8 Å.

Simple Description of the REDOR Experiment

Transverse magnetization which precesses about the static magnetic field due to dipolar interaction under the MAS condition moves back in the same direction at every rotor period because the integration of angular velocity (ω_D) due to dipolar interaction over one rotor period (T_r) is zero. Consequently, the rotational echo signals are refocused at each rotor period (Fig. 9.5b). When a π pulse is applied to the *S* nucleus, which is coupled with the *I* nucleus, in one rotor period, the pulse

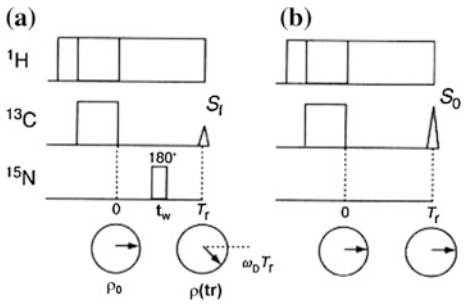

Fig. 9.5 Pulse sequence to observe rotational echo. **a** Transverse magnetizations of ^{13}C do not refocus at the rotor period in the REDOR pulse sequence. **b** Transverse magnetizations of ^{13}C refocus at the rotor period in the rotational echo pulse sequence without 180° pulse of ^{15}N

plays a role in inverting the precession direction of the magnetization of the observed I nucleus. Consequently, the magnetization vector of the I nucleus cannot move back in the same direction after one rotor period, and therefore, the amplitude of the echo intensity (S_f) decreases (Fig. 9.5a). The extent of the reduction of the rotational echo amplitude yields the interatomic distances. To evaluate the REDOR echo amplitude theoretically, one must consider the averaging precession frequency in the presence of a π pulse at the center of the rotor period over one rotor cycle as follows:

$$\begin{aligned}\overline{\omega_D(\alpha,\beta,t)} &= \mp\frac{1}{T_r}\left(\int_0^{\frac{T_r}{2}}\omega_D dt - \int_{\frac{T_r}{2}}^{T_r}\omega_D dt\right) \\ &= \pm\frac{D}{\pi}\sqrt{2}\sin 2\beta\sin\alpha\,,\end{aligned} \tag{9.10}$$

where α is the azimuthal angle and β is the polar angle defined by the internuclear vector with respect to the rotor axis system. Therefore, the phase angle, $\Delta\Phi(\alpha, \beta)$, for the N_c rotor cycle can be given by:

$$\Delta\Phi(\alpha,\beta) = \overline{\omega_D(\alpha,\beta,t)}N_c T_r, \tag{9.11}$$

where N_c is the number of rotor cycles and T_r is the rotor period. Finally, the echo amplitude can be obtained by averaging over every orientation, as follows;

$$S_f = \frac{1}{2\pi}\int_\alpha\int_\beta \cos[\Delta\Phi(\alpha,\beta)]d\alpha\sin\beta d\beta \tag{9.12}$$

Therefore, the normalized echo difference, $\Delta S/S_0$, can be given by:

$$\Delta S/S_0 = (S_0 - S_f)/S_0 \tag{9.13}$$

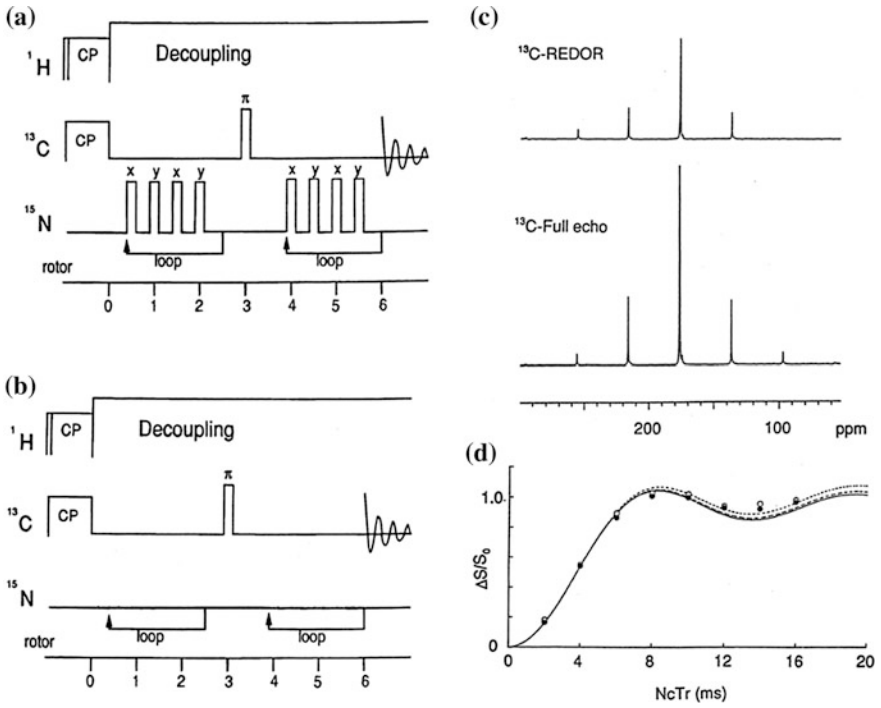

Fig. 9.6 **a** Pulse sequence for REDOR experiments. **b** Pulse sequence for full-echo experiments. **c** ^{13}C-REDOR and full-echo spectra of [1-^{13}C, ^{15}N]glycine. **d** $\Delta S/S_0$ plots against N_cT_r values

Experimentally, REDOR and full-echo spectra are acquired for a variety of N_cT_r values and respective REDOR (S_f) and full-echo (S_0) amplitudes are evaluated (Fig. 9.6).

Rotational Echo Amplitude by the Density Operator Approach

The REDOR echo amplitude can be evaluated more rigorously by using density matrix operators and a pulse sequence for the REDOR experiment, as shown in Fig. 9.5a [24]. The time evolution of the density operator, ρ_0, under heteronuclear dipolar interaction during one rotor period can be considered by taking the pulse length into account. The average Hamiltonian in the rotating frame over one rotor period can be given by:

$$
\begin{aligned}
\bar{\mathcal{H}} &= \frac{1}{T_\mathrm{r}}\left[\overline{\mathcal{H}_1(t)}\tau + \overline{\mathcal{H}_2(t)}t_\mathrm{W} + \overline{\mathcal{H}_3(t)}\tau\right] \\
&= \frac{D}{4\pi}\{\sin^2\beta[\sin(2\alpha+\omega_\mathrm{r}t_\mathrm{W}) + \sin(2\alpha-\omega_\mathrm{r}t_\mathrm{W}) - 2\sin 2\alpha] \\
&\quad 2\sqrt{2}\sin 2\beta[\sin\left(\alpha+\frac{1}{2}\omega_\mathrm{r}t_\mathrm{W}\right) + \sin\left(\alpha-\frac{1}{2}\omega_\mathrm{r}t_\mathrm{W}\right) + 2\sin 2\alpha] \\
&\quad -\sin^2\beta[\sin(2\alpha+\omega_\mathrm{r}t_\mathrm{W}) + \sin(2\alpha-\omega_\mathrm{r}t_\mathrm{W})]\frac{4\omega_\mathrm{r}^2 r_\mathrm{W}^2}{4\omega_\mathrm{r}^2 t_\mathrm{W}^2 - \pi^2} \\
&\quad +\sqrt{2}\sin 2\beta\left[\sin\left(\alpha+\frac{1}{2}\omega_\mathrm{r}t_\mathrm{W}\right) + \left(\alpha-\frac{1}{2}\omega_\mathrm{r}t_\mathrm{W}\right)\right]\frac{2\omega_\mathrm{r}^2 t_\mathrm{W}^2}{\omega_\mathrm{r}^2 t_\mathrm{W}^2 - \pi^2}\}I_Z S_Z \\
&\quad +\frac{D}{4\pi}\left\{\sin^2\beta[\cos(2\alpha+\omega_\mathrm{r}t_\mathrm{W}) + \cos(2\alpha-\omega_\mathrm{r}t_\mathrm{W})]\frac{2\pi\omega_\mathrm{r}t_\mathrm{W}}{4\omega_\mathrm{r}^2 t_\mathrm{W}^2 - \pi^2}\right. \\
&\quad \left.-\sqrt{2}\sin 2\beta\left[\cos\left(\alpha+\frac{1}{2}\omega_\mathrm{r}t_\mathrm{W}\right) + \cos\left(\alpha-\frac{1}{2}\omega_\mathrm{r}t_\mathrm{W}\right)\right]\frac{2\pi\omega_\mathrm{r}t_\mathrm{W}}{\omega_\mathrm{r}^2 t_\mathrm{W}^2 - \pi^2}\right\}I_z S_y \\
&= aI_z S_z + bI_z S_y
\end{aligned}
\tag{9.14}
$$

where $\overline{H_1}(t), \overline{H_2}(t)$ and $\overline{H_3}(t)$ are the average Hamiltonian corresponding to the period T_r shown in Fig. 9.5a. The pulse length, T_w, is also considered in calculations used to analyze REDOR results. The density operator, $\rho(T_\mathrm{r})$, at T_r after evolution under the average Hamiltonian can be calculated as

$$
\rho(T_\mathrm{r}) = \exp(-i\bar{H}T_\mathrm{r})\rho_0\exp(i\bar{H}T_\mathrm{r}), \tag{9.15}
$$

where ρ_0 is considered to be I_y after the contact pulse. The transverse magnetization at T_r can then be given by:

$$
\langle I_y(T_\mathrm{r})\rangle = T_\mathrm{r}\{\rho(T_\mathrm{r})I_y\} = \cos\left(\frac{1}{2}\sqrt{a^2+b^2}T_\mathrm{r}\right). \tag{9.16}
$$

Echo amplitude in powder sample can be calculated by averaging over all orientation as follows:

$$
S_\mathrm{f} = \frac{1}{2\pi}\int_\alpha\int_\beta \langle I_y(T_\mathrm{r})\rangle \sin\beta \mathrm{d}\beta\mathrm{d}\alpha, \tag{9.17}
$$

Therefore, the normalized echo difference, $\Delta S/S_0$, can be given by Eq. (9.13). When the length of τ_ω is zero, Eq. (9.16) can be simplified as follows:

$$\langle I_y(T_r)\rangle = \cos\left(\frac{D}{\pi}\sqrt{2}\sin 2\beta \sin \alpha T_r\right). \tag{9.18}$$

In this case, Eq. (9.17) is equivalent to Eq. (9.12) for $N_c = 1$.

Echo Amplitude in Three-Spin System (S_1-I_1-S_2)

It is important to consider the case where the observed nucleus (I_1) is coupled with two other heteronuclei (S_1 and S_2) [25]. The Hamiltonian in a three-spin system can be given by:

$$\begin{aligned} H(t) &= -\frac{\gamma_I\gamma_S h}{2\pi r_1^3}\left[3\cos^2\theta_1(t) - I\right]I_{Z1}S_{Z1} - \frac{\gamma_I\gamma_S h}{2\pi r_2^3}\left[3\cos^2\theta_2(t) - 1\right]I_{Z1}S_{Z2} \\ &= -D_1 I_{Z1}S_{Z1} - D_2 I_{Z1}S_{Z2}, \end{aligned} \tag{9.19}$$

where r_1 and r_2 are the I_1-S_1 and the I_1-S_2 interatomic distances, respectively. $\theta_1(t)$ and $\theta_2(t)$ correspond to the angles between the magnetic field and the I_1-S_1 and the I_1-S_2 internuclear vectors, respectively. In the molecular coordinate system, the x-axis is along the I_1-S_1 internuclear vector, and the S_1-I_1-S_2 plane is laid in the x-y plane. The angle between I_1-S_1 and I_1-S_2 is denoted by ζ. The coordinate system is transformed from the molecular axis system to the MAS system by applying a rotation transformation matrix $R(\alpha, \beta, \gamma)$ with Euler angles α, β, γ, followed by transforming from the MAS to the laboratory coordinate system by applying $R(\omega_1 t, \theta_m, 0)$. Finally, $\cos\theta_1(t)$ and $\cos\theta_2(t)$ are calculated as follows:

$$\begin{aligned} \cos\,\theta_1(t) = {} & (\cos\gamma\cos\beta\cos\alpha - \sin\gamma\sin\alpha)\sin\theta_m\cos\omega t \\ & - (\sin\gamma\cos\beta\cos\alpha + \cos\gamma\sin\alpha)\sin\theta_m\sin\omega t + \sin\beta\cos\alpha\cos\theta_m \end{aligned}$$

and

$$\begin{aligned} \cos\,\theta_2(t) = {} & [(\cos\gamma\cos\beta\cos\alpha - \sin\gamma\sin\alpha)\cos\zeta\sin\theta_m \\ & + (\cos\gamma\cos\beta\sin\alpha + \sin\gamma\cos\alpha)\sin\zeta\sin\theta_m]\cos\omega t \\ & - [(\sin\gamma\cos\beta\cos\alpha + \cos\gamma\sin\alpha)\cos\zeta\sin\theta_m \\ & + (\sin\gamma\cos\beta\sin\alpha - \cos\gamma\cos\alpha)\sin\zeta\sin\theta_m]\sin\omega t \\ & + \sin\beta\sin\alpha\cos\theta\sin\zeta + \sin\beta\sin\alpha\cos\theta_m\sin\zeta \end{aligned} \tag{9.20}$$

where θ_m is the magic angle between the spinner axis and the static magnetic field and ω_r is the angular variation of the spinner rotating about the magic-angle axis. The four resonance frequencies in the system are given by:

$$\begin{aligned}\omega_{D1} &= (D1-D2)/2\\ \omega_{D2} &= (D1+D2)/2\\ \omega_{D3} &= -(D1+D2)/2\\ \omega_{D4} &= -(D1-D2)/2\end{aligned} \tag{9.21}$$

These dipolar transition frequencies are time-dependent and repeat the cycle during spinning. In the REDOR pulse sequence, a π pulse is applied in the center of the rotor period. In this case, the averaged angular velocity over one rotor cycle for each resonance is given by:

$$\overline{\omega_i(\alpha,\beta,\gamma,t)} = \frac{1}{T_\mathrm{r}}\left(\int_0^{T_\mathrm{r}/2}\omega_{Di}\mathrm{d}t - \int_{T_\mathrm{r}/2}^{T_\mathrm{r}}\omega_{Di}\mathrm{d}t\right) \tag{9.22}$$

The phase accumulation after the N_c cycle is given by:

$$\Delta\Phi_i(\alpha,\beta,\gamma,t) = \overline{\omega_i(\alpha,\beta,\gamma,T_\mathrm{r})}N_\mathrm{C}T_\mathrm{r} \tag{9.23}$$

Finally, the ENDOR echo amplitude after averaging over all Euler angles is calculated as

$$S_\mathrm{f} = \frac{1}{8\pi^2}\sum_{i=1}^{4}\int_\alpha\int_\beta\int_\gamma[\cos\Delta\Phi_i(\alpha,\beta,\gamma,t)]\mathrm{d}\alpha\sin\beta\mathrm{d}\beta\mathrm{d}\gamma \tag{9.24}$$

The normalized echo difference, $\Delta S/S_0$, therefore strongly depends not only on the dipolar coupling of I_1-S_1 and I_1-S_2 but also on the angle S_1-I_1-S_2 [25].

Practical Aspects of a REDOR Experiment

It is emphasized that accurate interatomic distances are prerequisite to obtaining 3D structures of peptides, proteins, and macromolecules. Careful evaluation of the following points is the most important step to obtain reliable interatomic distances by REDOR experiments, although early paper did not necessarily take this into account. In practice, it is advisable to employ a standard sample such as [1-^{13}C] glycine [25], whose C–N interatomic distance was determined to be 2.48 A by a neutron diffraction study, to check that the correct parameters are set on spectrometer prior to beginning an experiment with the sample of interest.

The finite pulse length may affect the REDOR factor. Indeed, this effect is experimentally observed and can be calculated using Eq. (9.15). In one experiment, the REDOR parameter, $\Delta S/S_0$, was measured for 20% [1-^{13}C, ^{15}N]Gly. These values were plotted for the length of the ^{15}N π pulse [13.0 μs for the experiment and 24.6 μs (to satisfy 10% rotor cycle)] as a function of $N_\mathrm{c}T_\mathrm{r}$ with the calculated

lines using the π pulse length and finite length (13.0 and 24.6 μs) of the π pulse (Fig. 9.6D). It was found that the finite length of the ^{15}N π pulse does not significantly affect the REDOR effect provided that the pulse length is less than 10% of the rotor cycle at rotor frequency of 4000 Hz. Using a much faster spinning rate, radio frequency (rf) irradiation occupies a significant fraction of the rotor period (10–60%), and thus, the $\Delta S/S_0$ curve for REDOR deviates from that with an ideal δ-function pulse [26].

With most spectrometers, it is very difficult to eliminate fluctuations in rf power during the acquisition of REDOR experiments. It is, therefore, very important for the rf power to be stabilized after waiting a certain period as otherwise the π pulse will deviate with time from the exact π pulse. Consequently, the utility of REDOR for providing relatively long interatomic distances diminishes if the rf power changes. Instability of the rf power must be compensated for by the pulse sequence in order to eliminate long-term fluctuation of amplifiers. The xy-4 and xy-8 pulse sequences have been developed for this purpose, and the xy-8 pulse is the best sequence to compensate for fluctuations in rf power [27].

Since the initial development of the REDOR technique, contributions of natural abundance nuclei have been considered as the major source of error in distance measurement [28]. The observed dipolar interaction modified by the presence of neighboring naturally abundant nuclei was originally taken into account by simply calculating the $\Delta S/S_0$ values for the two isolated pairs and adding them proportionally to the natural abundance fraction [28]. Careful analysis of three-spin systems, however, indicates that this simple addition of the fraction in two-spin systems may result in serious overestimation of the natural abundance effect, yielding shorter distances [24]. Therefore, the most accurate way to address the natural abundance effect is to treat the whole spin system as a three-spin system by taking into account the neighboring carbons in addition to the labeled pair. In practice, contributions from naturally abundant nuclei can be ignored [25] for ^{13}C REDOR but not for ^{15}N REDOR, because the proportion of naturally abundant ^{13}C nuclei is much higher than that of ^{15}N nuclei.

^{13}C, ^{15}N-doubly labeled samples are typically used in REDOR experiment to determine the interatomic distances between labeled nuclei. However, the dipolar interaction between labeled ^{15}N nuclei in neighboring molecules should be taken into account as an additional factor contributing to the dipolar interaction of the pair under consideration. This contribution could be significant when the observed distance is quite large, because there are many contributions from nearby nuclei. This effect can be completely removed by diluting the labeled sample with a sample of the same compound with natural abundance of ^{13}C and ^{15}N. However, signal sensitivity will be sacrificed if the effect is to be completely removed, for example, by diluting the sample 1/49 [29]. Instead, it is advisable to evaluate the REDOR factors at infinitely diluted condition by extrapolating the data by stepwise dilution of the sample (i.e., 60, 30%) without losing sensitivity [25], given that a linear relationship between the REDOR factor and dilution can be ascertained by a theoretical consideration. Alternatively, the observed plots of $\Delta S/S_0$ values against the corresponding NcTr values for the undiluted sample can be fitted by a theoretical

curve obtained from dipolar interactions among three-spin systems. However, the accuracy of this latter approach is not always equivalent to that of a dilution experiment.

The transverse magnetization of REDOR experiment decays as a function of the ^{1}H decoupling field [30, 31]. Dipolar decoupling can be strongly hindered by molecular motion, if present, when the motional frequency is of the same order of magnitude as the decoupling field, thereby significantly shortening transverse relaxation times. Indeed, the T_2 value of the carbonyl carbons in crystalline Leu-enkephalin is very short due to the presence of backbone motion [32]. This is a serious problem in REDOR experiments, especially for long-distance pairs, because the signal-to-noise ratio (S/N) deteriorates significantly. In this case, it is worth considering measuring the ^{13}C REDOR signal under a strong decoupling field to elongate the transverse relaxation times. It is also useful to measure the distances at low temperature to reduce the motional frequency. It is cautioned, however, that crystalline phase transition could be associated with freezing of the solvent molecule as encountered using a variety of enkephalin samples [33].

The rotor of commercial NMR spectrometers is usually designed to allow as large sample volume as possible in order to achieve better sensitivity. This arrangement, however, can cause B_1 inhomogeneity, resulting in a broad distribution of lengths of the 90° pulses. This problem is serious in REDOR experiments in which a number of π pulses are applied, and pulse errors can accumulate during acquisition to give serious errors. In particular, the samples located at the top or bottom of the sample rotor feel a significantly weaker rf field [24, 34]. This greatly reduces the REDOR factor for samples which utilize the entire sample rotor, as is the case for cylindrical rotors. This effect should be seriously taken into account prior to conducting a REDOR experiment with a commercial spectrometer. It is, therefore, strongly recommended to fill only the center part of the coil with sample, just for a multiple-pulse experiment to acquire accurate interatomic distances as accurately as possible using the REDOR method.

9.2.2 Magic-Angle Spinning NMR

9.2.2.1 CP-MAS NMR

MAS NMR [35] seeks to mechanically average anisotropic interactions to obtain high-resolution spectra in which resonance is resolved on the basis of isotropic chemical shift and, in favorable cases, J-couplings. To achieve this, the sample is rotated rapidly (kHz) in a static magnetic field at an angle 54.7° (the magic angle). Since the anisotropic interactions that give rise to the broadening observed in the NMR spectra of solid materials possess a $(3\cos^2\theta - 1)/2$ dependence, a scaling of the anisotropic interaction is observed. When the sample rotation frequently exceeds the magnitude of the anisotropic interaction, this interaction is completely averaged and an anisotropic resonance is observed at its isotropic position.

When the sample rotation frequency is lower than that of the anisotropic interaction, incomplete averaging is lower than that of the anisotropic interaction. The resulting incomplete averaging is manifested in the solid-state NMR spectrum as a family of resonances separated from the isotropic resonance by multiples of the rotation frequency, known as spinning side bands.

Both ^{13}C and ^{15}N nuclei are frequently observed in membrane-associated peptides and proteins. CP techniques [36, 37] can thus be used to enhance the signal intensities of less abundant nuclei by transferring the polarization from abundant proton nuclei. Furthermore, combining CP, high-power proton decoupling, and MAS (CP-MAS) [38] enables the acquisition of high-resolution signals for biological molecules.

9.2.2.2 Correlation NMR Spectroscopy

The significant improvements in resolution afforded by MAS come at the expense of the information contained in the anisotropic interactions. A number of methods have thus been developed that permit selective reintroduction of these anisotropic interactions, thereby facilitating their analysis. These methods and their applications to biological systems have been extensively reviewed [4, 6].

The sequence of a protein backbone can be represented as C$\alpha(i)$–N(i)–CO($i + 1$)–C$\alpha(i + 1)$. Hence, to obtain sequential assignments using multidimensional correlation NMR, correlations must be established, for example, C$\alpha(i) \rightarrow$ N(i) $\rightarrow$ CO($i + 1$) (or vice versa). At the same time, the transfer should be restrained to this pathway to avoid misleading correlations over more than one amino acid. This is usually achieved using specific $^{13}C \leftrightarrow {}^{15}N$ CP techniques [39], which exploit a frequency-selected Hartmann–Hahn condition to reintroduce the heteronuclear dipolar ^{13}C–^{15}N coupling at a lower order, which implies that this method should also work with very fast spinning frequencies. In a specific CP experiment, chemical-shift-dependent transfer characteristics are introduced using a controlled frequency offset in combination with relatively weak rf fields on the heteronuclei. Alternatively, C$\alpha(i) \rightarrow$ N(i) $\rightarrow$ CO($i + 1$) correlations may be brought about using the proton-assisted intensive nuclei CP sequence [40], a third-spin-assisted recoupling-based method [41].

9.2.2.3 PDSD and DARR 2D NMR Spectroscopy

Single amino acids can be identified by means of their characteristic chemical shift and connectivity patterns, for example, between carbon resonances. A number of methods are available for reintroducing homonuclear dipolar ^{13}C–^{13}C couplings. A popular class of experiments relies on the proton-mediated reintroduction of carbon homonuclear dipolar couplings. This approach is usually referred to as longitudinal magnetization transfer by spin diffusion and facilitates zero-quantum flip-flop transition among ^{13}C nuclei. In its basic form, this process is known as

proton-driven spin diffusion (PDSD) [42]. In PDSD, the decoupling field on the proton channel is switched off (while ^{13}C magnetization is stored along the z-axis) during the spin diffusion mixing time to reintroduce heteronuclear dipolar couplings, thus increasing the efficiency of flip-flop transitions. This reintroduction occurs, however, only to higher order and scales inversely with the spinning frequency. Other methods, such as dipolar-assisted rotational resonance (DARR) [43, 44], the phase-alternated recoupling irradiation scheme [45], or mixed rotational and rotary resonance [46], outperform PDSD with increased spinning frequency because the heteronuclear dipolar couplings are reintroduced independent of the MAS frequency. However, because the flip-flop transition appears in the correlation terms of the effective Hamiltonian, the spin diffusion efficiency invariably decreases with increasing spinning frequency, although the transfer can still be efficient at very high MAS frequencies [47].

The DARR experiment can be used to determine the interatomic distance of carbon atoms as follows. First, spin diffusion among multiply labeled ^{13}C spins can be characterized by a master equation as follows [48, 49]:

$$M(\tau_m) = [\exp(-R\tau_m)]M(0), \tag{9.25}$$

where $M(\tau_m)$ represents the peak intensities for the labeled ^{13}C spins at the mixing time τ_m. $M(0)$ is the initial peak intensities for the diagonal components. The initial buildup rate $R_{j,k}$ for the direct polarization transfer can be given by [48]:

$$R_{j,k} = \frac{\gamma^4\hbar^2}{15}\left(\frac{1}{r_{jk}^{\text{eff}}}\right)^6\left(K_{ZQ}^{(j,k)}(\omega_R) + K_{ZQ}^{(j,k)}(-\omega_R) + \frac{1}{2}K_{ZQ}^{(j,k)}(2\omega_R) + \frac{1}{2}K_{ZQ}^{(j,k)}(-2\omega_R)\right) \tag{9.26}$$

$$\left(\frac{1}{r_{j,k}^{\text{eff}}}\right)^6 = \left(\sum_{m=1}^{Nj}\sum_{l=1}^{Nk}\frac{1}{r_{j,k,l,m}^6}\right) \tag{9.27}$$

where $K_{ZQ}^{(j,k)}$ and $r_{j,k,l,m}$ are the zero-quantum (ZQ) line-shape function and the distance between spin j in group l with N_l equivalent spins and spin k in group m with N_m equivalent spins. The zero-quantum line-shape function was calculated as [50, 51]:

$$K_{ZQ}^{(j,k)}(n\omega_R) = \frac{1}{2\pi}\int_{-\infty}^{\infty} F_j(\omega - n\omega_R)F_k(\omega)\mathrm{d}\omega \tag{9.28}$$

where $F_j(\omega)$ is the single-quantum (SQ) dipolar line-shape function of spin j under ^{13}C–^1H dipolar coupling with ^1H DARR recoupling field of MAS frequency, ω_R.

Thus, interatomic distances can be obtained from the $R_{j,k}$ value by varying the τ_m values using Eq. (9.25) in DARR experiment, and DARR interatomic distance $r_{j,k}^{DARR}$ can be obtained using Eqs. (9.26) and (9.27).

In PDSD and DARR experiments, dipolar truncation, which is the suppression of polarization transfer across small coupling by a larger coupling, does not strongly influence internuclear distances [52], and therefore, long internuclear distances are determined accurately. The effect due to multiple-spin labeling such as a change in transverse relaxation can be obtained by considering zero-quantum line-shape function [51].

9.3 Structure Determination of Membrane-Bound Peptides

The structures, topologies, and orientations of a number of membrane-bound peptides in lipid-bilayer environments have been investigated recently using solid-state NMR in order to understand their biological function. Solid-state NMR is particularly well suited for elucidating the dynamics, topologies, orientations, and high-resolution structures of peptides in bilayer environment using model and cell membranes. Peptides analyzed using this approach include venoms, antimicrobial peptides, and antibiotic peptides. In particular, chemical-shift oscillation analysis has allowed determination of the membrane-bound dynamic structures of melittin [7, 12, 53, 54], dynorphin [55], bombolitin [56], lactoferrampin [57], ECL-II of κ-opioid receptor [58], and alamethicin [59].

9.3.1 Melittin

Melittin, a hexacosapeptide with the primary structure Gly-Ile-Gly-Ala-Val-Leu-Lys-Val-Leu-Thr-Thr-Gly-Leu-Pro-Ala-Leu-Ile-Ser-Trp-Ile-Lys-Arg-Lys-Arg-Gln-Gln-NH_2, is the primary component of bee venom [60]. Melittin exhibits potent hemolytic activity [61] and induces voltage-dependent ion conductance across planar lipid bilayers at low concentration [62]. Melittin also causes selective micellization of lipid bilayers and membrane fusion at high concentrations [63]. As the temperature is lowered to approach the gel phase, the membrane breaks down into small particles. Upon raising the temperature above the gel-to-liquid crystalline phase-transition temperature (T_c), the small particles reform into unilamellar vesicles and ultimately into multilamellar vesicles. It has been proposed that bilayer disks surrounded by a belt of melittin molecules are formed at temperature below the Tc [64].

Giant vesicles with diameters of ∼20 μm were observed upon optical microscopic analysis of melittin–DMPC bilayers at 27.9 °C [12]. When the temperature

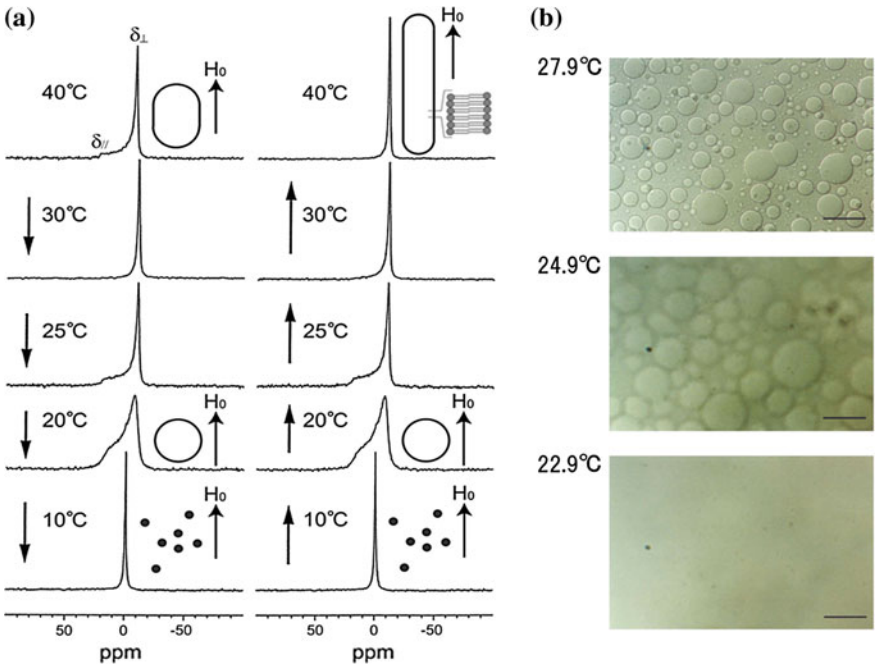

Fig. 9.7 **a** Effect of temperature variation on ^{31}P-NMR spectra of melittin–DMPC bilayer systems. *Arrows* indicate the direction of the temperature variation. H_0 indicates the direction of the static magnetic field. The shapes of the vesicles are also depicted on the right side of the spectra [53]. **b** Optical microscopic pictures of melittin–DMPC vesicle systems at 22.9, 24.9, and 27.9 °C [53]

was lowered to 24.9 °C (T_c = 23 °C for neat DMPC bilayers), the surface of the vesicles became blurred, and dynamic pore formation was visible in microscopic images collected at different exposure times (Fig. 9.7b) [53]. These vesicles disappeared completely at 22.9 °C. It was thus found that melittin–lecithin bilayer systems undergo reversible fusion and disruption near the respective T_c. The fluctuation of lipids is responsible for membrane fusion above the T_c, whereas the association of melittin molecules causes membrane lysis below the T_c.

Static ^{31}P dipolar-decoupled (DD)-MAS spectra of melittin–DMPC bilayers hydrated with Tris buffer were recorded at various temperatures (Fig. 9.7a) [53]. Immediately after the sample was placed in the magnetic field, the ^{31}P-NMR spectrum of an axially symmetric powder pattern characteristic of the liquid-crystalline phase was recorded at 40 °C. The upper field edge ($\delta_\perp$) was more intense than the lower field edge ($\delta_{//}$) as compared with a normal axially symmetric powder pattern. This finding indicates that the DMPC bilayer is partially aligned with the applied magnetic field, with the bilayer plane assuming a parallel orientation by forming elongated vesicles (Fig. 9.7a). When the temperature was lowered to 30 °C, the intensity of the upper field edge of the powder pattern increased further, leading to a spectrum exhibiting almost complete alignment with the

magnetic field. At 25 °C, the axially symmetric powder pattern appeared again. At 20 °C, this spectrum changed to a broad envelope of the powder pattern, with round edges due to the presence of a large-amplitude motion in addition to a rotational motion about the molecular axis associated with lateral diffusion of the lipid molecules. At 10 °C, the isotropic ^{31}P-NMR signal dominated near 0 ppm because of the isotropic rapid tumbling motion of small particles caused by melittin-induced lysis of the larger vesicles. The same axially asymmetric powder patterns reappeared when the temperature was raised from 10 to 25 °C as a result of fusion leading to the formation of larger spherical vesicles. At temperatures above 30 °C, a single perpendicular component at −12 ppm arose from the anisotropic ^{31}P chemical-shift tensor of the liquid-crystalline bilayer. This result indicates that the lipid-bilayer surface orients parallel to the magnetic field with a higher order of alignment by forming longer elongated vesicles, which are referred to as magnetically oriented vesicle systems (MOVS) [12].

Melittin-induced changes in the morphology of a lipid bilayer are illustrated in Fig. 9.8. Microscopic observation clearly indicated that at temperatures above the T_c, melittin binds strongly to the vesicles and is distributed homogeneously. At temperatures close to the T_c, melittin molecules associate with each other, resulting in phase separation, as observed by fluorescence microscopy. Consequently, a large-amplitude fluctuation of lipid molecules occurs near the T_c as shown in Fig. 9.8.

It was shown that melittin forms a pseudo-transmembrane amphiphilic α-helix [12]. However, melittin can remain in a homogeneous monomeric form in hydrophobic environments when the lipid bilayer enters the liquid-crystalline phase above the T_c. At temperatures close to the T_c, the hydrophilic sides of melittin molecules associate with one another such that the hydrophobic sides face the lipid molecules, which causes greater phase separation and partial disordering of the lipid bilayer. At temperature below the T_c, a large number of melittin molecules associate with each other. Consequently, small lipid-bilayer particles become surrounded by a belt of melittin molecules and are released from the vesicle, resulting in membrane disruption. Subsequently, entire vesicles dissolve in the buffer solution. At temperatures slightly above the T_c, a small number of associated melittin molecules may induce large-amplitude motion in liquid molecules in addition to motion about the molecular axis. This large-amplitude motion of lipid molecules may cause fluctuation on the surface of the vesicles, resulting in the mixing of lipids between adjacent vesicles and ultimately vesicle fusion.

Fully hydrated melittin–DMPC lipid bilayers also spontaneously align along a static magnetic field by forming elongated vesicles, with the long axis parallel to the magnetic field, as evidenced from static ^{31}P-NMR spectra (Fig. 9.7a). Using this magnetic orientation property of the membrane, the structure, orientation, and dynamics of melittin have been extensively studied [12]. Static ^{13}C-NMR spectra of [1-^{13}C]Ile4-melittin bound to a DMPG bilayer hydrated with Tris buffer recorded at −60 °C show a broad asymmetric powder pattern characterized by δ_{11} = 238, δ_{22} = 188, and δ_{33} = 112 ppm (with respect to TMS) (Fig. 9.1f). The presence of this broad signal indicates that any motion of melittin bound to the DMPG bilayer is

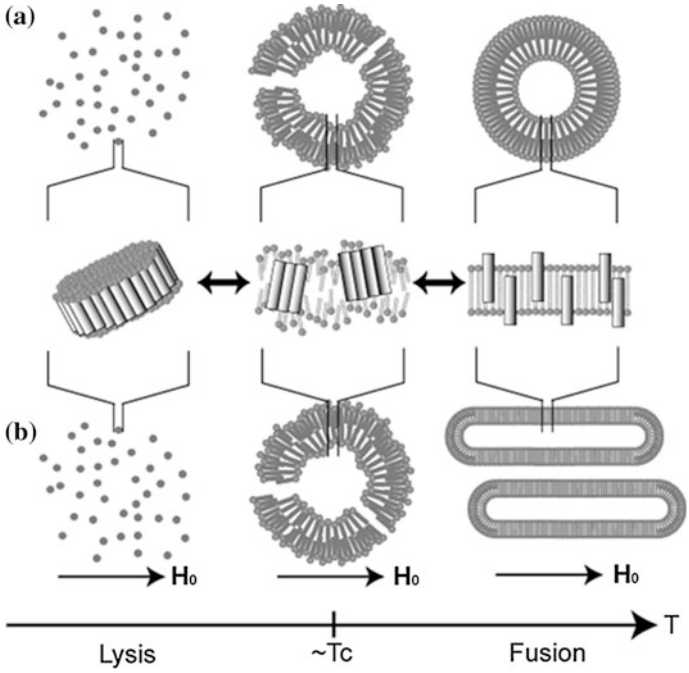

Fig. 9.8 Schematic representation of the process of morphological changes in melittin–lecithin bilayer systems in the absence (**a**) and presence (**b**) of an applied magnetic field [53]

completely frozen at −60 °C. A narrowed ^{13}C-NMR experiment conducted at 40 °C (Fig. 9.1h) showed melittin in the magnetically oriented state. An axially symmetric powder pattern with an anisotropy of 33.3 ppm was recorded at 40 °C in the corresponding slow DD-MAS experiment (Fig. 9.1g). Because the line width due to the anisotropy at 40 °C was not as broad as that at −60 °C, it was evident that the α-helical segment underwent rapid reorientation (>20 kHz) about the bilayer normal at 40 °C (Fig. 9.1c). The secondary structure of melittin bound to a DMPC bilayer can be determined based on conformation-dependent ^{13}C chemical shifts referenced to those of model system [65, 66]. The isotropic ^{13}C chemical shifts of the [1-^{13}C] Gly3, [1-^{13}C]Val5, [1-^{13}C]Gly12, [1-^{13}C]Leu16, and [1-^{13}C]Ile20 residues in melittin were determined to be 172.7, 175.2, 171.6, 175.6, and 174.8 ppm (with respect to TMS), respectively, indicating that all of these residues are involved in the α-helix [12].

The dynamic structure of melittin bound to MOVSs consisting of dipalmitoylphosphatidylcholine (DPPC) and dilauroylphosphatidylcholine (DLPC) was investigated by analyzing the ^{13}C anisotropic and isotropic chemical shifts of selectively ^{13}C-labeled carbonyl carbons of melittin under static and MAS conditions [7].

Axially symmetric chemical-shift powder patterns were observed for [1-^{13}C]Gly3, [1-^{13}C]Ala4, [1-^{13}C]Val5, [1-^{13}C]Gly12, [1-^{13}C]Leu16, and [1-^{13}C]Ile20. The lowest RMSDs were obtained at $\gamma_{G3} = 71° \pm 8°$ and $\zeta = 32° \pm 4°$ for the N-terminal α-helix (Gly3, Ala4, Val5) and $\gamma_{L16} = 80° \pm 6°$ and $\zeta = 30° \pm 3°$ for the C-terminal α-helix (Gly12, Leu16, Ile20) using Eq. (9.9). Practically, RMSD (γ, ζ)s were obtained by varying γ(0°–90°) and ζ(0°–180°) with respect to γG3 for the N-terminal α-helix and Leu16 for the C-terminal α-helix.

Based on the symmetry relationship expressed in Eq. (9.8), ζ or $-\zeta$ cannot be distinguished because of the $(3/2)\sin^2\zeta$ relation and γ and γ-180° cannot be distinguished because of the $\delta_{11}\cos^2\gamma + \delta_{33}\sin^2\gamma$ relation. Therefore, the possible (γ, ζ) combinations to show minimum RMSD value can be determined according to the following relationship:

$$\begin{aligned} \mathrm{RMSD}(\gamma, \zeta) &= \mathrm{RMSD}(\gamma - 180°, \zeta) \\ &= \mathrm{RMSD}(\gamma - 180°, -\zeta) \\ &= \mathrm{RMSD}(\gamma, -\zeta) \end{aligned} \tag{9.28}$$

For the N- and C-terminal helices in the melittin–DPPC bilayer systems, the lowest RMSD values are given by:

$$\begin{aligned} (\gamma_{G3}, \zeta)_N &= (+76°, \pm 36°) \text{ or } (-84°, \pm 36°) \quad \text{and} \\ (\gamma_{L16}, \zeta)_C &= (+82°, \pm 25°) \text{ or } (-98°, \pm 25°). \end{aligned} \tag{9.29}$$

In this case, the interatomic distance between [1-^{13}C]Val8 and [^{15}N]Leu13 was determined to be 4.8 Å by REDOR experiments [23, 67]. This distance allowed unique determination of the $(\gamma_{G3}, \zeta)_N$ = (+76°, −36°) and $(\gamma_{L16}, \zeta)_C$ = (−82°, +25°) values for melittin–DPPC bilayers, consistent with a larger kink angle (Fig. 9.9).

Analysis of the chemical-shift oscillation (Fig. 9.10) indicated that melittin molecules form two differently oriented α-helices and diffuse laterally to rotate rapidly around the membrane normal, with tilt angle for the N-terminal helix of −33° and −36° and 21° and 25° for the C-terminal helix in DLPC and DPPC vesicles, respectively (Fig. 9.8). The results provided interhelical angles of 126° and 119° in DLPC and DPPC membranes, respectively. These analyses led to the conclusion that the α-helices of melittin molecules penetrate the hydrophobic core of the bilayers incompletely as a pseudo-transmembrane structure, inducing fusion and disruption of the vesicles.

MD simulation for the melittin–DMPG system indicated that the basic residue Lys7 is located slightly within the lipid core region and interacts with one DMPG molecule to disturb the lower surface of the lipid bilayers, and this interaction is associated with melittin's membrane disruption activity (Fig. 9.7c) [54].

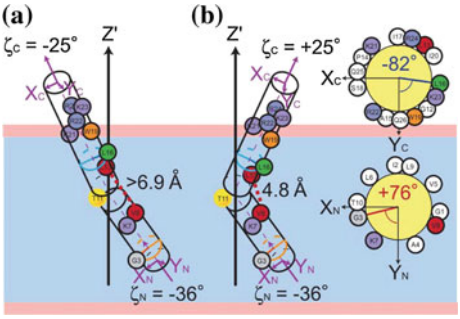

Fig. 9.9 Schematic representation of the possible structure of melittin bound to the DPPC vesicle from the analysis of the ^{13}C chemical-shift anisotropies. **a** $(\gamma_{G3},\zeta)_N = (+76°, -36°)$ and $(\gamma_{L16}, \zeta)_C = (-82°, -25°)$; **b** $(\gamma_{G3},\zeta)_N = (+76°, -36°)$ and $(\gamma_{L16}, \zeta)_C = (-82°, +25°)$; structure **b** is proved to be the actual structure based on the interatomic distance of 4.8 ± 0.2 Å, between [1-^{13}C]Val8 and [^{15}N]Leu13 of melittin bound to the DPPC bilayers, determined by the REDOR measurements. The helical wheel representation is illustrated in the helical molecular frame (HMF). The *Z*′-axis is the rotation axis of a melittin molecule, which is parallel to the membrane normal [7]

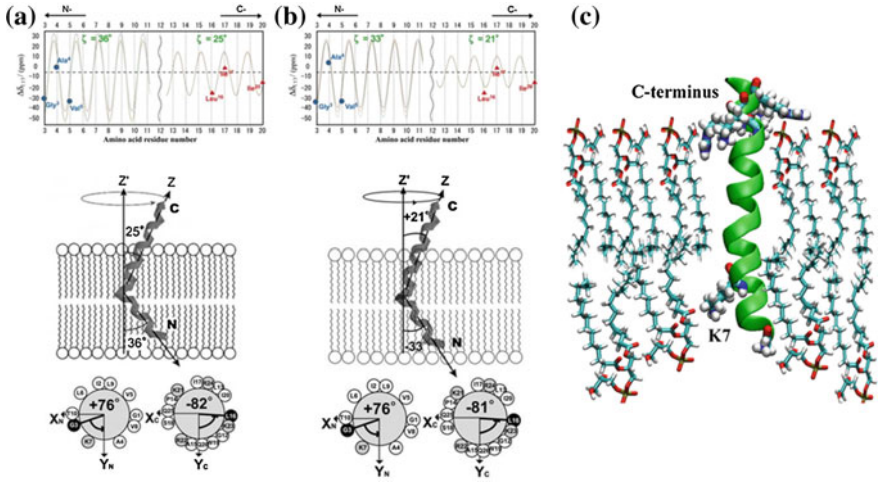

Fig. 9.10 Schematic representation of the structures and orientations of melittin. **a** Bound to DPPC and **b** DLPC lipid bilayers. *Top* Chemical-shift oscillation curves for [1-^{13}C]Gly3, Ala4, Val5, Leu16, Ile17, and Ile20 of melittin in DPPC (**a**) and DLPC (**b**) lipid bilayers. *Bottom* The N- and C-terminal helices of melittin bound to DPPC and DLPC lipid bilayers are inserted into the bilayer with the tilt angle of (36° and 33°) and (25° and 21°), respectively [4]. **c** Structure of melittin bound to DMPG bilayers obtained from MD simulation [54]

9.3.2 Alamethicin

Alamethicin is a 20-residue antibiotic peptide from *Trichoderma viride* [68]. The amino acid sequence is Ac-Aib-Pro-Aib-Ala-Aib-Ala-Gln-Aib-Val-Aib-Gly-Leu-Aib-Pro-Val-Aib-Aib-Gln-Gln-Phol in which 8 α-amino isobutyric acids (Aib) are included. In addition, the N-terminus is acetylated, and the C-terminus is terminated as an L-phenylalaninol residue [69]. Alamethicin consists of F30 and F50 types at a molar ratio of 0.85 and 0.12, respectively [70].

Alamethicin exhibits voltage-dependent ion channel activity in membranes [71]. Alamethicin has a high affinity for lipid bilayers and binds to the surface of lipid bilayers and inserts into the membrane. The orientation of alamethicin in a lipid bilayer depends upon the peptide-to-lipid (P/L) molar ratio [72], the type of lipid bilayer, and the membrane potential [73]. Various channel models have been proposed to determine its ion channel activity, such as the barrel-stave model [74]. Alamethicin channels are formed by parallel bundles of 3–12 transmembrane helical monomers surrounding a central water-filled pore [75]. The ion channel activity of alamethicin makes it a suitable model for investigating voltage-dependent ion channel proteins [76].

X-ray crystallographic data indicate that alamethicin assumes an overall helical structure with kink at Pro14, and the N- and C-termini assume α- and 3_{10}-helical structures, respectively [74]. Another study revealed that poly-Aib forms a 3_{10}-helix [77].

The conformation and orientation of membrane-bound alamethicin have been studied using solid-state NMR spectroscopy with DMPC/DHPC bicelle systems. Analysis of the ^{13}C chemical shifts of isotopically labeled alamethicin indicates that in lipid bilayers, the peptide forms an α-helical structure oriented along the bilayer normal [78].

The conformation of alamethicin in mechanically oriented phospholipid bilayers has been studied using ^{15}N solid-state NMR in combination with molecular modeling and MD simulations. Alamethicin variants labeled with ^{15}N at different positions in combination with substitution of three Aib residues with Ala residues were examined. Anisotropic ^{15}N chemical-shift data and ^{1}H–^{15}N dipolar couplings were determined for alamethicin with ^{15}N-labeled Ala6, Val9, and Val15 incorporated into a phospholipid bilayer at a peptide-to-lipid molar ratio of 1:8. This study indicated that alamethicin assumes a largely linear α-helical structure that spans the membrane, with the molecular axis tilted by 10–20° relative to the bilayer normal. In comparison, molecular modeling showed a straight α-helix tilted by 17°, and a slightly kinked MD structure was tilted by 11° relative to the bilayer normal [79]. Measurement of the orientation-dependent ^{1}H–^{15}N dipole–dipole coupling, ^{15}N anisotropic chemical shift, and ^{2}H quadrupole coupling parameters for a single residue, analysis of the anisotropic coupling parameters for a single residue, analysis of the anisotropic interaction for the Aib8 residue, and analysis of the anisotropic interaction for the Aib8 residue together provided detailed information

regarding the helix-tilt angle, wobble, and oscillatory rotation around the helical axis in the membrane-bound state of alamethicin [80].

Proton-decoupled ^{15}N solid-state spectra of a sample of alamethicin uniformly labeled with ^{15}N and reconstituted into oriented palmitoyloleoylphosphatidylcholine (POPC) and DMPC membranes showed that alamethicin adopts a transmembrane orientation upon reconstitution into the POPC-oriented membrane [81]. Two-dimensional ^{15}N chemical-shift ^{1}H–^{15}N dipolar-coupling solid-state NMR correlation spectroscopy (i.e., PISEMA) analysis suggested that in the transmembrane configuration, alamethicin adopts a mixed $\alpha/3_{10}$-helical structure with a tilt angle of 8.9° with respect to the bilayer normal [82].

Further detailed structural and orientational analyses of membrane-bound alamethicin have been carried out using solid-state NMR spectroscopy [4, 59]. ^{13}C chemical-shift interactions were observed in [1-^{13}C]-labeled alamethicin. The isotropic chemical-shift values indicated that the entire length of alamethicin forms a helical structure. The CSA of the carbonyl carbon of isotopically labeled alamethicin was also analyzed under the assumption that alamethicin molecules rotate rapidly about the bilayer normal of the phospholipid bilayer. It was concluded that the adjacent peptide plane forms an angle of 100° or 120° upon assumption of an α- or 3_{10}-helix, respectively. Anisotropic data were acquired for four and seven different residues at the N- and C-termini, respectively. The observed chemical-shift oscillation patterns for the ^{13}C CSAs of the carbonyl carbons are shown in Fig. 9.11. The chemical-shift oscillation pattern clearly indicated that there are two helices with different tilt angles. RMSD analysis indicated that the dihedral angles of adjacent peptide planes for the N- and C-termini were found to be 100° and 120°, respectively. It was, therefore, determined that the N- and C-termini form an α- and 3_{10}-helix, respectively (Fig. 9.11) [4, 59].

Hexagonal alamethicin ion channel model is illustrated in Fig. 9.11c, d, based on the previously obtained structure by MD simulation [79]. Membrane-bound structure of alamethicin determined by solid-state NMR analysis is used as a component of hexagonal alamethicin oligomer [59]. It is of interest to note that Gln7 and Gln18 residues face to the inside of the ion channel, and thus, the inside of the helical bundle shows hydrophilic character suggesting the high ion conductivity inside the channel.

9.3.3 Bovine Lactoferrampin

Bovine lactoferrampin (LFampinB) is a recently discovered 17-residue antimicrobial peptide with the sequence Trp-Lys-Leu-Leu-Ser-Lys-Ala-Gln-Glu-Lys-Phe-Gly-Lys-Asn-Lys-Ser-Arg. This peptide corresponds to residues 268-284 of N1 domain of the multifunctional glycoprotein bovine lactoferrin [83]. LFampinB exhibits more potent antimicrobial activity than lactoferrin and kills a wide variety of organisms, ranging from the yeast *Candida albicans* to a number of bacteria,

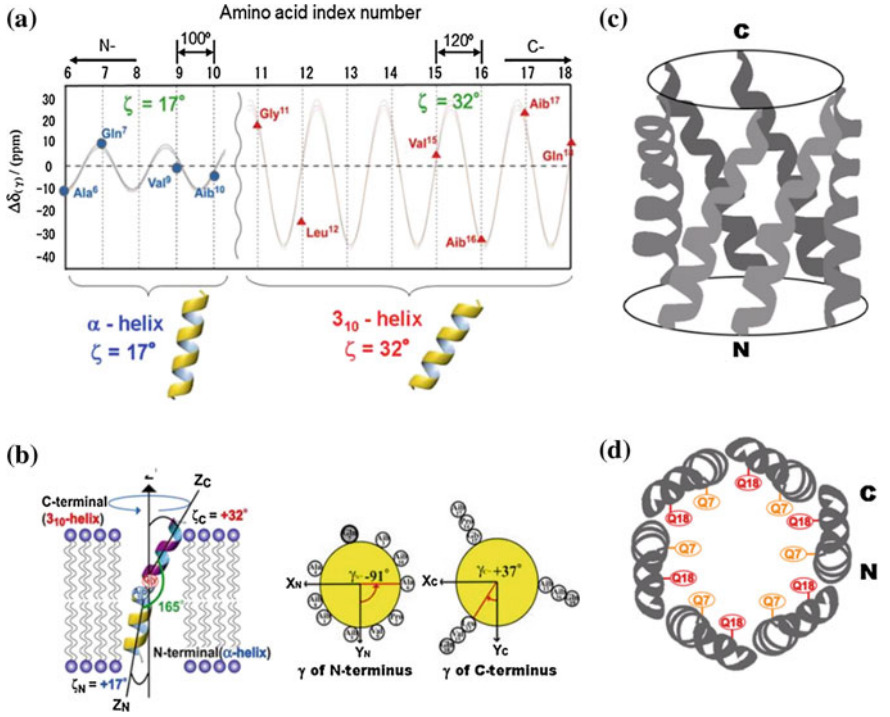

Fig. 9.11 **a** Chemical-shift oscillation patterns of alamethicin. Chemical-shift oscillation curves were obtained from the chemical-shift anisotropies of the N-terminus (Ala6, Gln7, Val9, and Aib10) and the C-terminus (Val15, Aib16, Aib17, and Gln18). The tilt angles of the N- and C-termini were determined as 17° and 32°, respectively. The dihedral angles of peptide planes between n and $n + 1$ residues of the N- and C-termini are analyzed to be α-helix and 3_{10}-helices, respectively. **b** Structure and topology of alamethicin bound to a DMPC bilayer, as determined from chemical-shift oscillation data [4, 59]. Side view (**c**) and top view (**d**) of hexameric oligomer of alamethicin in the membrane environment

including *Escherichia coli* [83–85]. LFampinB contains six basic amino acid residues and has a net charge of +5 at neutral pH. Solution-state NMR analysis revealed that LFampinB forms an amphipathic α-helix from the N-terminus to Phe11 and that the C-terminal region remains unstructured, when the peptide is bound to neutral and acidic micelles [86].

The antimicrobial activity of LFampinB is believed to result from membrane defects caused by interaction of the peptide with the bacterial membrane, although the molecular mechanism has yet to be completely elucidated. To date, four major models have been proposed to explain the antimicrobial activity of LFampinB: the "aggregate," "toroidal-pore," "barrel-stave," and "carpet" models (Fig. 9.12) [87]. In the aggregate model, peptides form a micelle-like structure with lipids and consequently translocate across the bilayer. In the toroidal-pore and barrel-stave models, the peptides orient in the transmembrane direction with respect to the

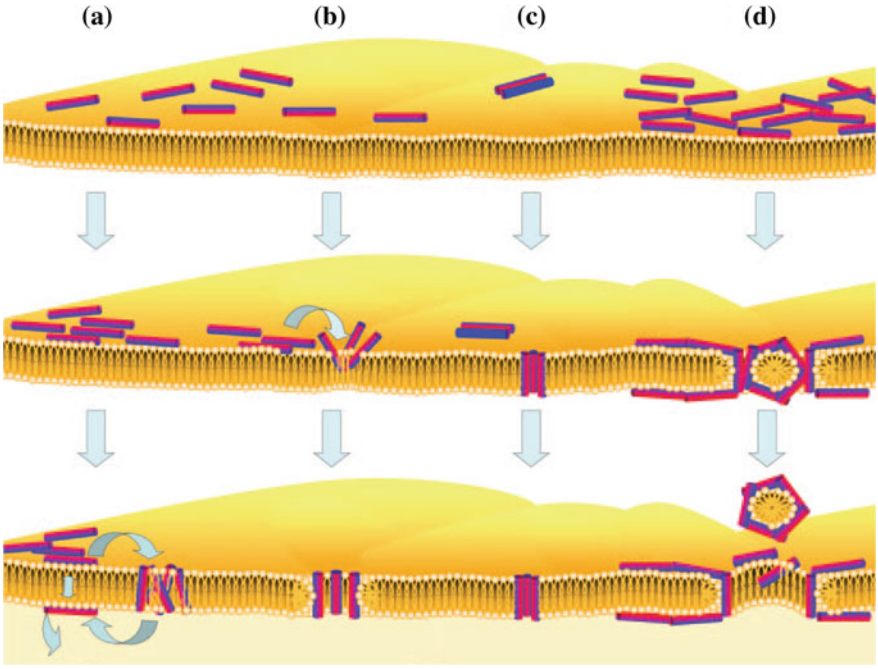

Fig. 9.12 Schematic representation of action of antimicrobial peptides to membrane. **a** Aggregate model (polyphemusin). **b** Toroidal-pore model (melittin, magainin). **c** Barrel-stave model (alamethicin). **d** Carpet model (ovispirin) [87]

membrane surface. In the toroidal-pore model, the lipid head groups are oriented so as to form a pore in the core of the membrane. In the barrel-stave model, the peptides align to the lipid direction and form a bundle with each other to provide a pore [88–90]. In the carpet model, peptides align along the surface of the lipid-bilayer plane [91]. The peptide exhibits detergent-like activity that creates a defect in the lipid bilayer. Bovine lactoferricin (LFcinB) interacts strongly with the bacterial membrane by forming a pore that disrupts the intracellular ion balance, in the same manner as LFampinB derived from the N1-domain of lactoferrin [92]. Analysis of an antimicrobial peptide's structure and orientation with respect to the membrane surface is therefore important to gain insight into its antimicrobial activity.

^{13}C- and ^{31}P-NMR measurements, and ^{13}C-^{31}P REDOR experiments, and potassium ion-selective electrode and quartz-crystal microbalance analyses were carried out for LFampinB bound to mimetic bacterial membrane [57]. The ^{31}P-NMR results indicated that LFampinB causes a defect in the mimetic bacterial membrane. Ion-selective electrode measurements showed that ions leak from mimetic bacterial membrane containing cardiolipin. Quartz-crystal microbalance measurements revealed that LFampinB has a greater affinity for acidic than for neutral phospholipids. ^{13}C DD-MAS and static NMR spectra showed that

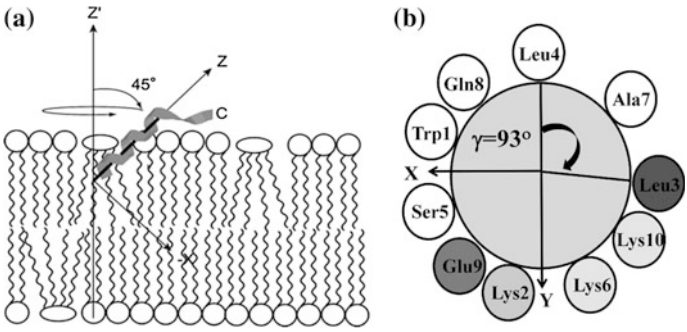

Fig. 9.13 Schematic representation of membrane-bound structure for LFampinB. **a** Most probable alignment and structure bound to bacterial membrane. **b** Helix wheel and plane angle for carbonyl carbons. *X*-axis indicates the direction from bilayer normal to the helix axis. Carbonyl plane normal shows 93° from the *Y*-axis [57]

LFampinB forms an α-helix in the N-terminal region and is tilted 45° relative to the bilayer normal. Dephasing patterns of the carbonyl carbon nucleus in LFampinB and the phosphorus nuclei of lipid phosphate groups were determined using ^{13}C-^{31}P REDOR and revealed that LFampinB localized in the interfacial region of the membrane (Fig. 9.13). MD simulations showed a tilt angle of 42° and a rotation angle of 92.5° for Leu3, both of which were in excellent agreement with experimental values [57].

9.4 Structure Determination of Membrane Proteins

Membrane proteins embedded in biological membranes account for 30% of the proteins encoded in the human genome and play an essential role in maintaining the homeostasis of cells, and knowledge of the structure of membrane proteins is extremely important to understanding their function. However, only about 1–2% of experimentally determined protein structures registered in the Protein Data Bank are membrane proteins. Solid-state NMR spectroscopy can provide structural information associated with the conformation, orientation, and dynamics of even insoluble biological macromolecules such as membrane proteins. Solid-state NMR spectroscopy does not require crystallization and is not restricted by the upper limits to molecular weight that affect X-ray crystallography and in solution NMR methods. Consequently, solid-state NMR can be directly applied to studies of the structure of membrane proteins reconstituted in lipid bilayers, over a broad range of lipid compositions, temperature, and pH. High-resolution structures of membrane proteins have recently been determined using MAS methods [93–97]. The structure of the G-protein-coupled chemokine receptor CXCR1 in liquid-crystalline phospholipid bilayers was determined using rotationally aligned NMR spectroscopy [93]. The trimeric structure of the transmembrane domain of the auto-transporter

adhesion protein YadA using the transmembrane domain of YadA in microcrystals was determined using solid-state MAS NMR [94]. This section reviews the high-resolution structures of various membrane proteins determined by solid-state MAS NMR analyses.

In solid-state NMR analyses of membrane proteins with slow tumbling motion in lipid environments, both spectral resolution and signal intensity are strongly affected by anisotropic spin interactions such as CSA, and by homo- and heteronuclear dipolar interactions. CP-MAS involving high-power proton decoupling can yield high-resolution solid-state NMR spectra for membrane protein samples. For sequential assignments and distance constraints of membrane protein structures, recoupling techniques can be combined with multidimensional NMR experiment under MAS conditions. PDSD involves spin diffusion between coupled ^{13}C spins in the presence of dipolar coupling with a ^{1}H spin bath [42, 98]. The technique was used to determine the 3D structure of selectively isotope-labeled SH3 protein without attenuation of long-distance correlations by dipolar truncation induced by strong dipolar coupling such as ^{13}C–^{13}C direct bonds [99]. DARR described by Takegoshi et al. [43, 44] induced spin diffusion between ^{13}C spins enhanced by rf irradiation of the ^{1}H spins with the same amplitude as the MAS frequency [43]. Consequently, under DARR conditions, the effects of dipolar truncation can be avoided even for uniformly labeled proteins, enabling the determination of long-range correlation [44, 100, 101]. DARR, as well as other recoupling techniques, can contribute significantly to the determination of sequential assignments and correlation of long-distance constraints in membrane protein structural analysis when combined with multidimensional NMR techniques. In addition, ^{13}C–^{13}C correlations based on dipolar interactions are also useful for determining distances between a ligand and neighboring residues of a membrane protein. The visual pigment rhodopsin containing the retinal chromophore is a member of the G-protein-coupled receptors (GPCRs) family. Upon the absorption of light, rhodopsin containing 11-*cis* retinal changes to meta-rhodopsin II (Meta II) with an all-*trans* configuration and a deprotonated Schiff base. This configurational change causes significant structural changes in the residues around the retinal chromophore. Smith et al. have been focusing on Tyr Cζ in bovine rhodopsin and have shown alteration of cross-peaks between ^{13}C-labeled retinal, Met $^{13}C\varepsilon$, and Tyr $^{13}C\zeta$. These NMR results identified the structural changes in the protein during the process of photo-activation [102, 103]. ^{13}C–^{13}C correlations have also been used to characterize structure of the retinal-binding pocket in microbial rhodopsin. *Krokinobacter* rhodopsin 2 (KR2) from the marine flavobacteria *Krokinobacter eikastus* functions as a light-driven sodium ion pump, and its crystal structure under acidic condition has been determined [104]. Structural differences in the retinal-binding pocket of KR2 reconstituted into POPE/POPG membranes at acidic and neutral pH conditions were recently revealed using DARR NMR and ^{15}N CP-MAS techniques [105]. DARR spectra obtained using a mixing time of 500 ms showed cross-peaks between retinal ^{13}C-14, retinal ^{13}C-20, Lys255 $^{13}C\varepsilon$, and Tyr218 $^{13}C\zeta$ (Fig. 9.14a). KR2 has 15 Tyr residues, and the interatomic distance between Cζ of Tyr218 and the C20 methyl carbon in retinal is within 5 Å.

The crystal structure data show that the next closest tyrosine is very far from C20 retinal [104]. Thus, the DARR spectra observed the cross-peak of Tyr218 in contact with retinal. The ^{15}N NMR spectrum showed an unusual chemical-shift value of the protonated Schiff base in KR2, indicating that KR2 has an all-*trans* retinal configuration and a twist around the N-Cε bond. In addition, Tyr218 near the retinal formed a relatively weak hydrogen bond with Asp251. Apart from ^{15}N Schiff base signal, the chemical-shift values of retinal ^{13}C-14, retinal ^{13}C-20, Lys255 ^{13}Cε, and Tyr218 ^{13}Cζ did not change under acidic condition (Fig. 9.14b), indicating that interaction between the protonated Schiff base and counter-ion is the main change in the retinal-binding pocket between acidic and neutral conditions.

Signal assignments of membrane proteins usually begin as a record of ^{13}C–^{13}C intraresidue correlations used to identify amino acids through side-chain correlation patterns. Adequate resolution of C–C correlations is key to a successful structure determination experiment, because the 5–70 ppm aliphatic region is the fingerprint region for residue types. Well-resolved ^{13}C–^{13}C correlations have recently been reported for a number of membrane proteins, including YadA [94], the potassium channel KcsA-Kv1.3 [106], human aquaporin-1 [107], DsbB [96], proteorhodopsin [108, 109], and sensory rhodopsin II (SRII) [110]. NCOCX (for inter-residue),

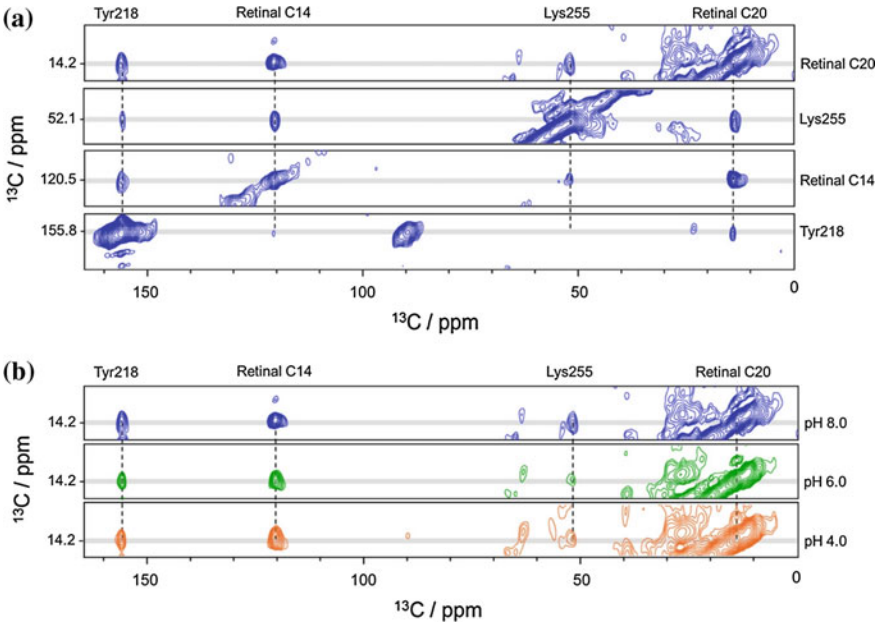

Fig. 9.14 ^{13}C–^{13}C DARR spectra of wild-type KR2 in a POPE/POPG membrane in a Tris–NaCl solution. **a** Correlation peaks of labeled residues at pH 8.0. Cross-peaks and diagonal peaks are represented by the *gray line*. **b** Comparison of cross-peaks at pH 8.0 (*top*, *blue*), pH 6.0 (*middle*, *green*), and pH 4.0 (*bottom*, *orange*). All columns show correlations with retinal C20. Cross-peaks and diagonal peaks are represented by the *gray line* [105]

NCACX (for intraresidue), and CONCA (for inter-residue) with ^{13}C–^{13}C correlation have been used to construct spin systems for individual amino acid residues and connect the spin systems along the amino acid sequence. Dipolar-coupling data determined using recoupling technique, such as PDSD and DARR, can provide interatomic distances for structural constraints. ^{13}C-based conformation-dependent chemical-shift tables can be used to correlate isotropic chemical shifts of amino acid residues with site-specific secondary structures [65, 66]. Backbone torsion angle (ϕ and ψ) can be estimated from corrected chemical shifts in sequential assignments using TALOS+ (torsion-angle likelihood obtained from shift and sequence similarity) software [111]. Structural calculations based on a large number of torsion-angle constraints and interatomic distances, together with the RMSD for backbone atoms, can provide an ensemble of structures.

Anabaena sensory rhodopsin (ASR) from Anabaena sp. PCC 7120 is a photoreceptor comprising seven-transmembrane helices and a retinal chromophore. ASR is believed to function in chromatic adaptation together with a soluble transducer protein [112]. The atomic resolution fine structure of ASR was recently determined using attentive solid-state MAS NMR spectroscopy. Uniformly and sparsely isotopically labeled ASR in DMPC/DMPA lipid bilayers provided high-resolution solid-state MAS NMR spectra at 800 MHz [95]. Well-resolved correlated peaks with high S/N ratios and narrow line width of 0.5 ppm were observed in 2D DARR ^{13}C–^{13}C correlated spectra of uniformly labeled ASR (Fig 9.15) [113], indicating that the ASR sample was stable and characterized by excellent structural homogeneity in the membranes. ^{15}N CP-MAS analysis indicated an all-trans configuration of retinal.

Sequential assignments for ASR were obtained using NCACX and NCOCX with DARR optimal short mixing times and CONCA from a single sample. The sequential assignments for the BC loop region in ASR are shown in Fig. 9.16. Although the X-ray structure of ASR [114] lacks the BC loop region, there are two short β-strands. Around 90% of the backbone and amino acid side chains could be assigned in experiments involving sparsely labeled ASR [95, 113, 115]. The water-accessible surface and transmembrane domain of the protein, as well as light-induced conformational changes, were characterized through H/D exchange experiments. The light-induced conformational changes occur in the cytoplasmic halves of helices F and G and at the ends of helices B and C [113, 116].

TALOS was used to determine dihedral restraints (186 ϕ and ψ pairs) from conformation-dependent N, C′, Cα, and Cβ chemical shifts in ASR. Excellent spectral resolution allowed determination of a number of short, medium, and long interatomic distances by PDSD, CHHC, and a homogeneously broadened rotational resonance (HBR2) [117, 118]. In addition, paramagnetic relaxation enhancement (PRE) experiments with cross-linking, along with circular dichroism (CD) experiments, provided structural insights regarding trimer formation in lipid bilayers and intermonomer distance restraints based on interfacial contacts [119]. Starting from a calculated low-resolution template structure, a total of 1390 short- and 435 medium-range internuclear distances, long-range interhelical constraints, retinal–proton contacts, and intra- and intermonomer PREs with dihedral constrains

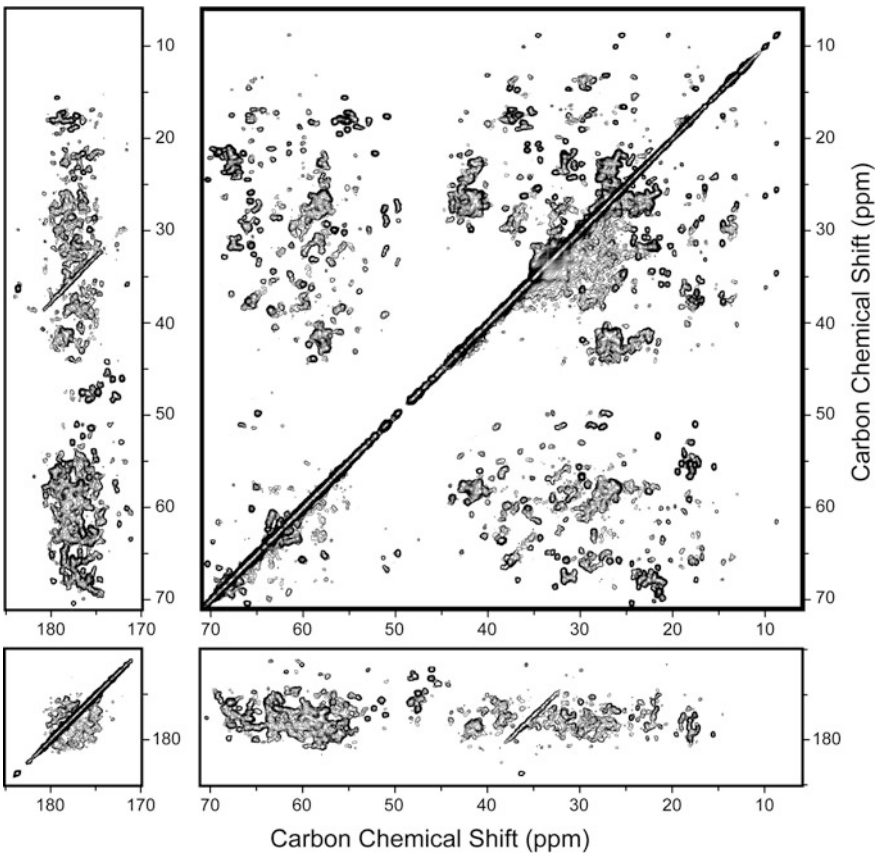

Fig. 9.15 2D ^{13}C–^{13}C correlation spectrum of *Anabaena* sensory rhodopsin (*ASR*) using solid-state NMR spectrometer at 800 MHz [113]

were used in the structural calculation [95] (Fig. 9.16). As a result, an ensemble of 10 structures was obtained with a backbone RMSD of 0.6 Å. This detailed trimeric structure of ASR in lipid environments differs notably from the crystal structure (Fig. 9.17). This structure will no doubt enhance understanding of the mechanism of the interaction between ASR (monomer) and the soluble transducer protein.

9.5 Conclusion

It is demonstrated that membrane-bound peptide rotates rapidly about the bilayer normal. Based on this dynamic structure characteristic of membrane-bound peptide, chemical-shift oscillation analyses can provide a detailed picture of the structure and orientation of membrane-bound peptides as combined with accurate

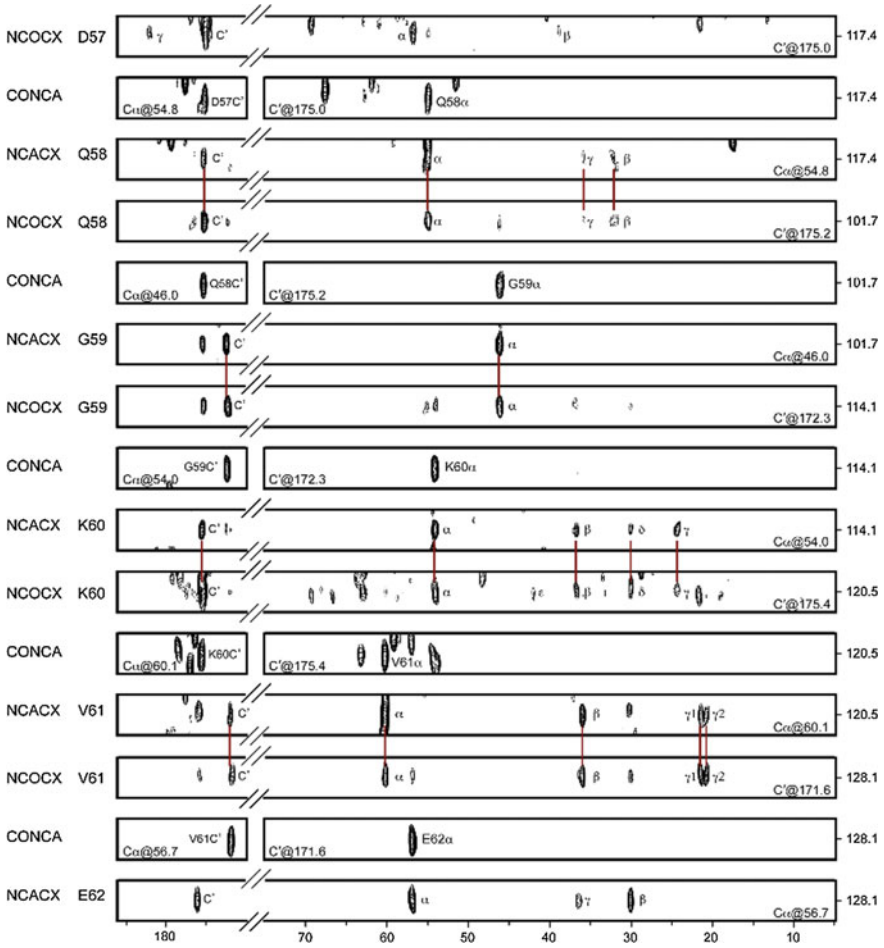

Fig. 9.16 Sequential assignment from Asp57 to Glu62 in the BC loop of Anabaena sensory rhodopsin (ASR) [113]

internuclear distances. Using solid-state NMR analysis, melittin showed pseudo-transmembrane bending α-helical structure which induces fusion and disruption of the vesicles. Membrane-bound alamethicin was found to be bending transmembrane structure, and the N- and C-termini form an α- and 3_{10}-helices, respectively. When hexagonal alamethicin oligomer channels are considered, Gln7 and Gln18 residues face to the inside of the channels that explain high ion conductivity of the ion channels. MAS NMR spectroscopy provides high-resolution NMR signals which permit the assignments of the nuclei in the particular amino acid residues. The chemical shifts and internuclear distance constraints can be used to determine the high-resolution structure of membrane proteins ASR to be trimer form in lipid environments.

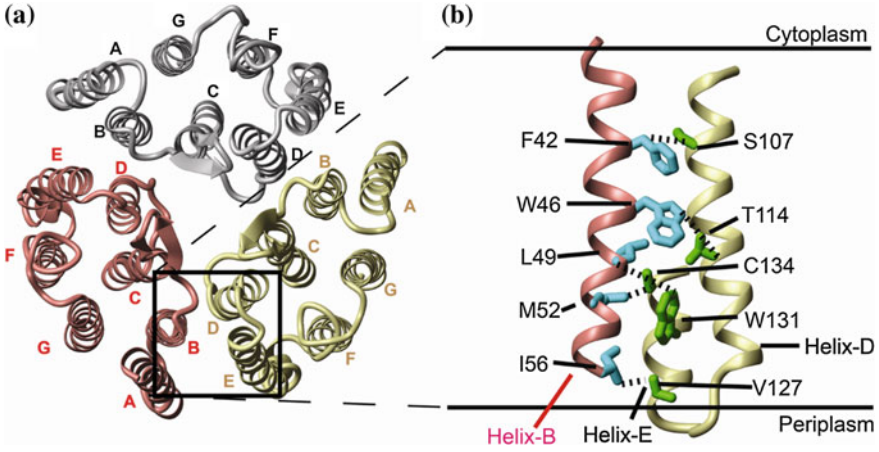

Fig. 9.17 **a** Top view and **b** side view of the square part of the structure of *Anabaena* sensory rhodopsin (*ASR*) trimer, as determined by solid-state MAS NMR technique [95]

Acknowledgements This work was supported by grants-in-aid for Scientific Research in an Innovative Area (16H00756 to AN and 16H00828 to IK) and by a grant-in-aid for Scientific Research (C) (15K06963 to AN) and Research (B) (15H04336 to IK) from the Ministry of Education, Culture, Sports, Science and Technology of Japan.

References

1. Opella, S.J., Marassi, F.M.: Structure determination of membrane proteins by NMR spectroscopy. Chem. Rev. **104**, 3587–3606 (2004)
2. Watts, A., Straus, S.K., Grage, S.L., Kamihira, M., Lam, Y.H., Zhao, X.: Membrane protein structure determination using solid-state NMR. In: Downing, A.K. (ed.) Protein NMR. Techniques, methods in molecular biology, vol. 278, pp. 403–473. Humana Press, Totowa (2004)
3. Saitô, H., Ando, I., Naito, A.: NMR constraints for determination of secondary structure. In: Solid state NMR spectroscopy for biopolymers. Principles and Applications, pp. 127–199. Springer, Berlin (2006)
4. Naito, A.: Structure elucidation of membrane-associated peptides and proteins in oriented bilayers by solid-state NMR spectroscopy. Solid State Nucl. Magn. Reson. **36**, 67–76 (2009)
5. Opella, S.J., Das, B.B.: Determination of the equivalence of solid-state NMR orientational constraints from magnetic and rotational alignment of the coat protein in a filamentous bacteriophage. In: Separopvic, F., Naito, A. (eds.) Advances in Biological Solid State NMR: Protein and Membrane-Active Peptides, pp. 53–70. Royal Society of Chemistry, Cambridge (2014)
6. Naito, A., Kawamura, I., Javkhlantugs, N.: Recent Solid-state NMR studies of membrane-bound peptides and proteins. Annu. Rev. NMR Spectrosc. **86**, 333–411 (2015)
7. Toraya, S., Nishimura, K., Naito, A.: Dynamic structure of vesicle-bound melittin in a variety of lipid chain lengths by solid-state NMR. Biophys. J. **87**, 3323–3335 (2004)

8. Marassi, F.M., Ramamoorthy, A., Opella, S.J.: Complete resolution of the solid-state NMR spectrum of a uniformly ^{15}N-labeled membrane protein in phospholipid bilayers. Proc. Natl. Acad. Sci. **94**, 8551–8556 (1997)
9. Opella, S.J.: Solid-state NMR and membrane ptoteins. J. Magn. Reson. **253**, 129–137 (2015)
10. Weingarth, M., Buldus, M.: Introduction to Biological Solid-State NMR: Protein and Membrane Active Peptides, pp. 1–17. Royal Society of Chemistry, Cambridge (2014)
11. Ward, M.E., Brown, L.S., Ladizhansky, V.: Advanced solid-state NMR techniques for characterization of membrane protein structure and dynamics: application to anabaena sensory rhodopsin. J. Magn. Reson. **253**, 119–128 (2015)
12. Naito, A., Nagao, T., Norisada, K., Mizuno, T., Tuzi, S., Saitô, H.: Conformation and dynamics of melittin bound to magnetically oriented lipid bilayers by solid-state ^{31}P and ^{13}C NMR spectroscopy. Biophys. J. **78**, 2405–2417 (2000)
13. Wu, C.H., Ramamoorth, A., Opella, S.J.: High-resolution heteronuclear dipolar solid-state NMR spectroscopy. J. Magn. Reson. **A109**, 270–272 (1994)
14. Ramamoorthy, A., Wei, Y., Lee, D.-K.: PISEMA solid-state NMR spectroscopy. Annu. Rep. NMR Spectrosc. **52**, 1–52 (2004)
15. Lee, D.K., Narasimhaswamy, T., Ramamoorthy, A.: PITANSEMA, a low-power PISEMA solid-state NMR experiment. Chem. Phys. Lett. **399**, 359–362 (2004)
16. Nishimura, K., Naito, A.: Dramatic reduction of the RF power for attenuation of sample heating in 2D-separated local field solid-state NMR spectroscopy. Chem. Phys. Lett. **402**, 245–250 (2005)
17. Nishimura, K., Naito, A.: Remarkable reduction of rf power by ATANSEMA and DATANSEMA separated local field in solid-state NMR spectroscopy. Chem. Phys. Lett. **419**, 120–124 (2006)
18. Gor'kov, P.L., Chekmenev, E.Y., Li, C., Cotton, M., Butfy, J.J., Traasch, N.J., Veglia, G., Brey, W.W.: Using low-E resonance to reduce RF heating in biological samples for static solid-state NMR up to 900 MHz. J. Magn. Reson. **185**, 77–93 (2007)
19. Yamamoto, K., Lee, D.K., Ramamoorthy, A.: Spectroscopy, broadband-PISEMA solid-state NMR spectroscopy. Chem. Phys. Lett. **407**, 289–293 (2005)
20. Marassi, F.M., Opella, S.J.: A solid-state NMR index of helical membrane protein structure and topology. J. Magn. Reson. **144**, 150–155 (2000)
21. Marrasi, F.M., Ma, C., Gesel, J.J., Opella, S.J.: Three-dimensional solid-state NMR spectroscopy is essential for resolution of resonances from in-plane residues in uniformly ^{15}N-labeled helical membrane proteins in oriented lipid bilayers. J. Magn. Reson. **144**, 156–161 (2000)
22. Wang, J., Denny, J., Tian, C., Kim, S., Mo, Y., Kovacs, F., Song, Z., Nishimura, K., Gan, Z., Fu, R., Quine, J.R., Cross, T.A.: Imaging membrane protein helical wheels. J. Magn. Reson. **144**, 162–167 (2000)
23. Gullion, T., Schaefer, J.: Rotational-echo double-resonance. J. Magn. Reson. **81**, 196–200 (1989)
24. Naito, A., Nishimura, K., Kimura, S., Tuzi, S., Aida, M., Yasuoka, N., Saitô, H.: Determination of the three-dimensional structure of a new crystalline form of N-acetyl-Pro-Gly-Phe as revealed by ^{13}C REDOR, X-ray diffraction, and molecular dynamics calculation. J. Phys. Chem. **100**, 14995–15004 (1996)
25. Naito, A., Nishimura, K., Tuzi, S., Saitô, H.: Inter- and intra-molecular contributions of neighboring dipolar pairs to the precise determination of interatomic distances in a simple [^{13}C, ^{15}N]-peptide by ^{13}C, ^{15}N-REDOR NMR spectroscopy. Chem. Phys. Lett. **229**, 506–511 (1994)
26. Jaroniec, C.P., Tounge, B.T., Rienstra, C.M., Herzfeld, J., Griffin, R.G.: Recoupling of heteronuclear dipolar interactions with rotational-echo double-resonance at high magic-angle spinning frequencies. J. Magn. Reson. **146**, 132–139 (2000)
27. Gullion, T., Schaefer, J.: Elimination of resonance offset effects in rotational-echo double resonance NMR. J. Magn. Reson. **92**, 439–442 (1991)

28. Pan, Y., Gullion, T., Schaefer, J.: Determination of C-N internuclear distances by rotational-echo double-resonance NMR of solids. J. Magn. Reson. **90**, 330–340 (1990)
29. Garbow, J.R., McWherter, C.A.: Determination of the molecular conformation of melanostatin using ^{13}C, ^{15}N-REDOR NMR spectroscopy. J. Am. Chem. Soc. **115**, 238–244 (1993)
30. Suwelack, D., Rothwell, W.P., Waugh, J.S.: Slow molecular motion detecting in the NMR spectra of rotating solids. J. Chem. Phys. **74**, 2559–2569 (1980)
31. Rothwell, W.P., Waugh, J.S.: Transverse relaxation of dipolar coupled spin systems under rf irradiation. J. Chem. Phys. **74**, 2721–2732 (1981)
32. Naito, A., Fukutani, A., Uitdehaag, M., Tuzi, S., Saitô, H.: Backbone dynamics of polycrystalline peptides studied by measurements of ^{15}N NMR lineshapes and ^{13}C transverse relaxation times. J. Mol. Struct. **441**, 231–241 (1998)
33. Kamihira, M., Naito, A., Nishimura, K., Tuzi, S., Saitô, H.: A high-resolution solid-state ^{13}C and ^{15}N NMR study on crystalline Leu- and Met-enkephalins: Distinction of polymorphs, backbone dynamics and local conformational rearrangements induced by dehydration or freezing of motion of bound solvent molecules. J. Phys. Chem. B **102**, 2826–2834 (1998)
34. Peersen, O.B., Groesbeek, M., Aimoto, S., Smith, S.O.: Analysis of rotational resonance magnetization exchange curves from crystalline peptides. J. Am. Chem. Soc. **117**, 7228–7237 (1995)
35. Andrew, E.R.: The narrowing of NMR spectra of solids by high-speed specimen rotation and resolution of chemical shift and spin multiplet structure for solids. Prog. Nucl. Magn. Reson. Spectrosc. **8**, 1–39 (1971)
36. Hartmann, S.R., Hahn, E.L.: Nuclear double resonance in the rotating frame. Phys. Rev. **128**, 2042–2053 (1962)
37. Pines, A., Gibby, M.G., Waugh, J.S.: Proton-enhanced NMR of dilute spins in solids. J. Chem. Phys. **59**, 569–590 (1973)
38. Schaefer, J., Stejeskal, E.O.: Carbon-13 nuclear magnetic resonance of polymers spinning at magic angle. J. Am. Chem. Soc. **98**, 1031–1032 (1976)
39. Baldus, M., Petokova, A.T., Herzfeld, J., Griffin, R.G.: Cross polarization in the tilted frame assignment and spectral simplification in heteronuclear spin system. Mol. Phys. **95**, 1197–1207 (1998)
40. Lewandowski, J.R., Paep, G.D., Griffin, R.G.: Proton assisted insensitive nuclei cross polarization. J. Am. Chem. Soc. **129**, 728–729 (2007)
41. Paep, G.D., Lewandowski, J.R., Loquet, A., Bockmann, A., Griffin, R.G.: Proton assisted recoupling and protein structure determination. J. Chem. Phys. **129**, 245101 (2008)
42. Grommek, A., Meier, B.H., Ernst, M.: Distance information from proton-driven spin diffusion under MAS. Chem. Phys. Lett. **427**, 631–637 (2006)
43. Takegoshi, K., Nakamura, S., Terao, T.: ^{13}C–^{1}H dipolar-assisted rotational resonance in magic-angle spinning NMR. Chem. Phys. Lett. **344**, 631–637 (2001)
44. Takegoshi, K., Nakamura, S., Terao, T.: ^{13}C–^{1}H dipolar-driven ^{13}C–^{13}C recoupling without ^{13}C rf irradiation in nuclear magnetic resonance of rotating solids. J. Chem. Phys. **118**, 2325–2341 (2003)
45. Weingarth, M., Demaco, D.E., Bodenhausen, G., Tekely, P.: Improved magnetization transfer in solid-state NMR with fast magic angle spinning. Chem. Phys. Lett. **469**, 342–348 (2009)
46. Scholz, I., Huber, M., Manolikas, T., Meier, B.H., Ernst, M.: MIRROR recoupling and its application to spin diffusion under fast magic-angle spinning. Chem. Phys. Lett. **460**, 278–283 (2008)
47. Weigarth, M., Masuda, Y., Takegoshi, K., Bodenhausen, G., Tekely, P.: Sensitive ^{13}C–^{13}C correlation spectra of amyloid fibrils at very high spinning frequencies and magnetic fields. J. Biomol. NMR **50**, 129–136 (2011)
48. Egawa, A., Fujiwara, T., Mizoguchi, T., Kakitani, Y., Koyama, Y., Akutsu, H.: Structure of the light-harvesting bacteriochlorophyll c assembly in chlorosomes from *Chlorobium limicola* determined by solid-state NMR. Proc. Natl. Acad. Sci. **104**, 790–795 (2007)

49. Dumez, J.L., Emsley, L.: A master-equation approach to the description of proton-driven spin diffusion from crystal geometry using simulated zero-quantum lineshapes. Phys. Chem. Chem. Phys. **13**, 7363–7370 (2011)
50. Kubo, A., McDowell, C.A.: Spectral spin diffusion in polycrystalline solids under magic angle spinning. Chem. Soc. Faraday Trans. I **84**, 3713–3730 (1988)
51. Kubo, A., McDowell, C.A.: ^{31}P spectral spin diffusion in crystalline solids. J. Chem. Phys. **89**, 63–70 (1988)
52. Grommek, A., Meier, B.H., Ernst, M.: Distance information from proton-driven spin diffusion under MAS. Chem. Phys. Lett. **427**, 404–409 (2006)
53. Toraya, S., Nagao, T., Norisada, K., Tuzi, S., Saitô, H., Izumi, S., Naito, A.: Morphological behavior of lipid bilayers induced by melittin near the phase transition temperature. Biophys. J. **89**, 3214–3222 (2005)
54. Norisada, K., Javkhlantugs, N., Mishima, D., Kawamura, I., Saitô, H., Ueda, K., Naito, A.: Dynamic structure and orientation of melittin bound to acidic lipid bilayers, as revealed by solid-state NMR and molecular dynamics simulation. J. Phys. Chem. B **121**, 1802–1811 (2017)
55. Uezono, T., Toraya, S., Obata, M., Nishimura, K., Tuzi, S., Saitô, H., Naito, A.: Structure and orientation of dynorphin bound to lipid bilayers by ^{13}C solid-state NMR. J. Mol. Struct. **749**, 13–19 (2005)
56. Toraya, S., Javkhlantugs, N., Mishima, D., Nishimura, K., Ueda, K., Naito, A.: Dynamic structure of bombolitin II bound to lipid bilayers as revealed by solid-state NMR and molecular-dynamics simulation. Biophys. J. **99**, 3282–3289 (2010)
57. Tsutsumi, A., Javkhlantugs, N., Kira, A., Umeyama, M., Kawamura, I., Nishimura, K., Ueda, K., Naito, A.: Structure and orientation of bovine lactroferrampin in the mimetic bacterial membrane as revealed by solid-state NMR and molecular dynamic simulation. Biophys. J. **103**, 1735–1743 (2012)
58. Kira, A., Javkhlantugs, N., Miyamori, T., Sasaki, Y., Eguchi, M., Kawamura, I., Ueda, K., Naito, A.: Interaction of extracellular loop II of k-opioid receptor (196–228) with opioid peptide dynorphin in membrane environments as revealed by solid state nuclear magnetic resonance, quartz crystal microbalance and molecular dynamics simulation. J. Phys. Chem. B **2014**(118), 9604–9612 (2014)
59. Nagao, T., Mishima, D., Javkhlantugs, N., Wang, J., Ishioka, D., Yokota, K., Norisada, K., Kawamura, I., Ueda, K., Naito, A.: Structure and orientation of antibiotic peptide alamethicin in phospholipid bilayers as revealed by chemical shift oscillation analysis of solid state nuclear magnetic resonance and molecular dynamics simulation. Biochim. Biophys. Acta **2015**(1848), 2789–2798 (2015)
60. Habermann, E., Jentsc, J.: Sequence analysis of melittin from tryptic and peptic degradation and products. Hoppe-Seyler's Z. Phys. Chem. **348**, 37–50 (1967)
61. Sessa, G., Free, J.H., Colacicco, G., Weissmann, G.: Interaction of a lytic polypeptide, melittin, with lipid membrane systems. J. Biol. Chem. **244**, 3575–3582 (1969)
62. Tosteson, M.T., Tosteson, D.C.: The sting melittin forms channels in lipid bilayers. Biophys. J. **36**, 109–116 (1981)
63. Dempsey, C.E.: The action of melittin on membrane. Biochim. Biophys. Acta **1031**, 143–161 (1990)
64. Dufourcq, J., Faucon, J.-F., Fourche, G., Dasseux, J.L., Le Maire, M., Gulik-Krywicki, T.: Morphological change of phosphatidylcholine bilayers induced by melittin: vesicularization, fusion, discoidal particles. Biochim. Biophys. Acta **859**, 33–48 (1986)
65. Saitô, H.: Conformation-dependent ^{13}C chemical shifts: a new means of conformation characterization as obtained by high-resolution solid-state ^{13}C NMR. Magn. Reson. Chem. **24**, 835–852 (1986)
66. Saitô, H., Ando, I.: High-resolution solid-state NMR studies of synthetic and biological macromolecules. Annu. Rep. NMR Spectrosc. **21**, 209–290 (1989)
67. Naito, A., Saitô, H.: Limit of accuracy of internuclear distances measured by REDOR. Encycl. Nucl. Magn. Reson. **9**, 191–283 (2002)

68. Meyer, C.E., Reusser, F.: A polypeptide antibacterial agent isolated from *Trichoderma viride*. Experientia **23**, 85–86 (1967)
69. Balasubramanian, T.M., Kendrick, N.C.E., Taylor, M., Marshall, G.R., Hall, J.E., Vodyanoy, J., Reusser, F.: Synthesis and characterization of the major component of alamethicin. J. Am. Chem. Soc. **103**, 6127–6132 (1981)
70. Vedovato, N., Baldhini, C., Toniolo, C., Rispoli, G.: Pore-forming properties of alamethicin F50/5 inserted in a biological membrane. Chem. Biodivers. **4**, 1338–1346 (2007)
71. Mueller, P., Rudin, D.O.: Action potentials induced in biomolecular lipid membranes. Nature **217**, 713–719 (1068)
72. Dave, P.C., Billington, E., Pan, Y.-L., Straus, S.K.: Interaction of alamethicin with ether-linked phospholipid bilayers: oriented circular dichroism, ^{31}P solid-state NMR, and differential scanning calorimetry studies. Biophys. J. **89**, 2434–2442 (2005)
73. Tieleman, D.P., Berendsen, H.J.C., Sanson, M.S.P.: Voltage-dependent insertion of alamethicin at phospholipid/water and octane/water interfaces. Biophys. J. **80**, 331–346 (2001)
74. Fox Jr., R.O., Richards, F.M.: A voltage-gated ion channel model inferred from the crystal structure of alamethicin at 1.5-Å resolution. Nature **300**, 325–330 (1982)
75. Pan, P., Tristram-Nagle, S., Nagle, J.F.: Alamethicin aggregation in lipid membranes. J. Membr. Biol. **231**, 11–27 (2009)
76. Sansom, M.S.: Alamethicin and related peptaibols—model ion channels. Eur. Biophys. J. **22**, 105–124 (1993)
77. Saitô, H., Tabeta, R., Formaggio, F., Crisma, M., Toniolo, C.: High-resolution solid-state ^{13}C-NMR of peptides: A study of chain-length dependence for 3_{10}-helix formation. Biopolymers **27**, 1607–1617 (1988)
78. Nagao, T., Naito, A., Tuzi, S., Saitô, H.: Conformation and orientation of biologically active peptide alamethicin in phospholipid bilayer by high-resolution solid state NMR spectroscopy. Pept. Sci. **1988**, 341–344 (1988)
79. Bak, M., Bywater, R.P., Hohwy, M., Thomsen, J.K., Adelhorst, K., Jakobsen, H.J., Søronsen, O.W., Nielsen, N.C.: Conformation of alamethicin in oriented phospholipid bilayers determined by ^{15}N solid-state nuclear magnetic resonance. Biophys. J. **81**, 1684–1698 (2001)
80. Bertelsen, K., Paaske, B., Thøgersen, L., Tajkhorshid, E., Schiøtt, B., Skrydstrup, T., Nielsen, N.C., Vosegaard, T.: Residue-specific information about the dynamics of antimicrobial peptides from ^{1}H–^{15}N and ^{2}H solid-state NMR spectroscopy. J. Am. Chem. Soc. **131**, 18335–18342 (2009)
81. Bechinger, B., Skladnev, D.A., Ogrel, A., Li, X., Rogozhkina, E.V., Ovchinnikova, T.V., O'Neil, J.D.J., Raap, J.: ^{15}N and ^{31}P solid-state NMR investigations on the orientation of Zervamicin II and alamethicin in phosphatidylcholine membranes. Biochemistry **40**, 9428–9437 (2001)
82. Salnikov, E.S., Friedrich, H., Li, X., Bertani, P., Reissmann, S., Hertweck, C., O'Neil, J.D.J., Raap, J., Bechinger, B.: Structure and alignment of the membrane-associated peptaibols ampullosporin A and alamethicin by oriented ^{15}N and ^{31}P solid-state NMR spectroscopy. Biophys. J. **96**, 86–100 (2009)
83. van der Kraan, M.I.A., Groenink, J., Nazmi, K., Veeman, E.C.I., Bolscher, J.G.M., Amerongen, A.V.N.: Lactoferrampin: A novel antimicrobial peptide in the N1-domain of bovine lactoferrin. Peptides **25**, 177–183 (2004)
84. van der Kraan, M.I.A., van Marle, J., Nazmi, K., Groenink, J., van't Hof, W., Veerman, E.C. I., Bolscher, J.G.M., Amerongen, A.V.N.: Ultrastructural effects of antimicrobial peptides from bovine lactoferrin on the membranes of *Candida albicans* and *Escherichia coli*. Peptides **26**, 1537–1542 (2005)
85. van der Kraan, M.I.A., Nazmi, K., Teeken, A., Groenink, J., van't Hof, W., Veeman, E.C.I., Bolscher, J.M.G., Amerongen, A.V.N.: Lactoferrampin, an antimicrobial peptide of bovine lactoferrin, exerts its candidacidal activity by a cluster of positively charged residues at the

C-terminus in combination with a helix-facilitating N-terminal part. Biol. Chem. **386**, 137–142 (2005)
86. Haney, E.F., Lau, F., Vogel, H.J.: Solution structure and model membrane interactions of lactoferrampin, an antimicrobial peptide derived from bovine lactoferrin. Biochim. Biophys. Acta **1768**, 2355–2364 (2007)
87. Jenssen, H., Hamill, P., Hancock, R.E.W.: Peptide antimicrobial agents. Clin. Microbiol. Rev. **19**, 491–511 (2006)
88. Matsuzaki, K., Murase, O., Fujii, N., Miyajima, K.: An antimicrobial peptide, magainin 2, induced rapid flip-flop of phospholipids coupled with pore formation and peptide translocation. Biochemistry **35**, 11361–11368 (1996)
89. Katherine, A., Wildman, H., Lee, D.-K., Ramamoorthy, A.: Mechanism of lipid bilayer disruption by the human antimicrobial peptide, LL-37. Biochemistry **42**, 6545–6558 (2003)
90. Steve, K.H., Ludtke, L., Worcester, D.L., Huang, H.W.: Neutron scattering in the plane of membranes: structure of alamethicin pores. Biophys. J. **1996**(70), 2659–2666 (1996)
91. Pouny, Y., Rapaport, D., Mor, A., Nicolas, P., Shai, Y.: Interaction of antimicrobial dermaseptin and its fluorescently labeled analogues with phospholipid membranes. Biochemistry **31**, 12416–12423 (1992)
92. Umeyama, M., Kira, A., Nishimura, K., Naito, A.: Interaction of bovine lactoferricin with acidic phospholipid bilayers and its antimicrobial activity as studied by solid-state NMR. Biochim. Biophys. Acta **1758**, 1523–1528 (2006)
93. Park, S.H., Das, B.B., Casagrande, F., Tian, F.Y., Nothnagel, H.J., Chu, M., Kiefer, H., Maier, K., De Angelis, A.A., Marassi, F.M., Opella, S.J.: Structure of the chemokine receptor CXCR1 in phospholipid bilayers. Nature **491**, 779–783 (2012)
94. Shahid, S.A., Bardiaux, B., Franks, W.T., Krabben, L., Habeck, M., van Rossum, B.-J., Linke, D.: Membrane-protein structure determination by solid-state NMR spectroscopy of microcrystals. Nat. Methods **9**, 1212–1217 (2012)
95. Wang, S., Munro, R.A., Shi, L., Kawamura, I., Okitsu, T., Wada, A., Kim, S.-Y., Jung, K.-H., Brown, L.S., Ladizhansky, V.: Solid-state NMR spectroscopy structure determination of a lipid-embedded heptahelical membrane protein. Nat. Methods **10**, 1007–1012 (2013)
96. Tang, M., Nesbill, A.E., Sperling, L.J., Berthold, D.A., Schwieters, C.D., Gennis, R.B., Rienstra, C.M.: Structure of the disulfide bond generating membrane protein DsbB in the lipid bilayer. J. Mol. Biol. **425**, 1670–1682 (2013)
97. Traaseth, N.J., Shi, L., Verardi, R., Mullen, D.G., Barany, G., Veglia, G.: Structure and topology of monomeric phospholamban in lipid membranes determined by a hybrid solution and solid-state NMR approach. Proc. Natl. Acad. Sci. USA **106**, 10165–10170 (2009)
98. Suter, D., Ernst, R.R.: Spin diffusion in resolved solid-state NMR spectra. Phys. Rev. **32**, 5608–5627 (1985)
99. Castellani, F., van Rossum, B., Diehl, A., Schubert, M., Rehbein, K., Oschkinat, H.: Structure of a protein determination by solid-state magic-angle-spinning NMR spectroscopy. Nature **420**, 98–102 (2002)
100. Crocker, E., Patel, A.B., Eilers, M., Jayaraman, S., Getmanova, E., Reeves, P.J., Ziliox, M., Khorana, H.G., Sheves, M., Smith, S.O.: Dipolar assisted rotational resonance NMR of tryptophan and tyrosine in rhodopsin. J. Biomol. NMR **29**, 11–20 (2004)
101. Marulanda, D., Tasayco, M.L., Cataldi, M., Arriaran, V., Polenova, Y.: Resonance assignments and secondary structure analysis of *E. coli* thioredoxin by magic spinning solid-state NMR spectroscopy. J. Phys. Chem. B **109**, 18135–18145 (2005)
102. Eilers, M., Goncalves, J.A., Ahuja, S., Kirkup, C., Hirshfeld, A., Simmerling, C., Reeves, P. J., Sheves, M., Smith, S.O.: Structural transitions of transmembrane helix 6 in the formation of metarhodopsin I. J. Phys. Chem. B **116**, 10477–10489 (2012)
103. Kimata, N., Pope, A., Eilers, M., Opefi, C.A., Ziliox, M., Hirshfeld, A., Zaitseva, E., Vogel, R., Sheves, M., Reeves, P.J., Smith, S.O.: Retinal orientation and interactions in rhodopsin reveal a two-stage trigger mechanism for activation. Nat. Commun. **7**, 12683 (2016)
104. Kato, H.E., Inoue, K., Abe-Yoshizumi, R., Kato, Y., Ono, H., Konno, M., Hososhima, S., Ishizuka, T., Hoque, M.R., Kunitomo, H., Ito, J., Yoshizawa, S., Yamashita, K., Takemoto,

M., Nishizawa, T., Taniguchi, R., Kogure, K., Maturana, A.D., Iino, Y., Yawo, H., Ishitani, R., Kandori, H., Nureki, O.: Structural basis for Na^+ transport mechanism by a light-driven Na^+ pump. Nature **521**, 48–53 (2015)
105. Shigeta, A., Ito, S., Inoue, K., Okitsu, T., Wada, A., Kandori, K., Kawamura, I.: Solid-state nuclear magnetic resonance structural study of the retinal-binding pocket in sodium ion pump rhodopsin. Biochemistry **56**, 543–550 (2017)
106. Lange, A., Giller, K., Hornig, S., Martin-Eauclaire, M.-F., Pongs, O., Becker, S., Baldus, M.: Toxin-induced conformational changes in a potassium channel revealed by solid-state NMR. Nature **440**, 959–962 (2006)
107. Emami, S., Fan, Y., Munro, R., Ladizhansky, V., Brown, L.S.: Yeast-expressed human membrane protein aquaporin-1 yields excellent resolution of solid-state MAS NMR spectra. J. Biomol. NMR **55**, 147–155 (2013)
108. Yang, J., Aslimovska, L., Glaubitz, C.: Molecular dynamics of proteorhodopsin in lipid bilayers by solid-state NMR. J. Am. Chem. Soc. **133**, 4874–4881 (2011)
109. Shi, L., Ahmed, M.A.M., Zhang, W., Whited, G., Brown, L.S., Ladizhansky, V.: Three-dimensional solid-state NMR study of a seven-helical integral membrane proton pump-structure insights. J. Mol. Biol. **386**, 1078–1093 (2009)
110. Etzkom, M., Seidel, K., Li, L., Martell, S., Geyer, M., Engelhard, M., Baldus, M.: Complex formation and light activation in membrane-embedded sensory rhodopsin II as seen by solid-state NMR spectroscopy. Structure **18**, 293–300 (2010)
111. Shen, Y., Delaglio, F., Cornilescua, G., Bax, Ad: TALOS+: a hybrid method for predicting protein backbone torsion angles from NMR chemical shifts. J. Biomol. NMR **44**, 213–223 (2009)
112. Jung, K.-H., Trivedi, V.D., Spudich, J.L: Demonstration of a sensory rhodopsin in eubacteria. Mol. Microbiol. **47**, 1513–1522 (2003)
113. Shi, L., Kawamura, I., Jung, K.-H., Brown, L.S., Ladizhansky, V.: Conformation of a seven-helical transmembrane photosensor in the lipid environment. Angew. Chem. Int. Ed. **50**, 1302–1305 (2011)
114. Vogeley, L., Sineshchekov, O.A., Trivedi, V.D., Sasaki, J., Spudich, J.L., Luecke, H.: Anabaena sensory rhodopsin: a photochromic color sensor at 2.0 Å. Science **306**, 1390–1393 (2004)
115. Wang, S., Shi, L., Okitsu, T., Wada, A., Brown, L.S., Ladizhansky, V.: Solid-state NMR ^{13}C and ^{15}N resonance assignments of a seven-transmembrane helical protein Anabaena Sensory Rhodopsin. Biomol. NMR Assign **7**, 253–256 (2013)
116. Wang, S., Shi, L., Kawamura, I., Brown, L.S., Ladizhansky, V.: Site-specific solid-state NMR detection of hydrogen-deuterium exchange reveals conformational changes in a 7-helical transmembrane protein. Biophys. J. **101**, L23–L25 (2011)
117. Peng, X., Libich, D., Janik, R., Harauz, G., Ladizhansky, V.: Dipolar chemical shift correlation spectroscopy for homonuclear carbon distance measurements in proteins in the solid state: application to structure determination and refinement. J. Am. Chem. Soc. **130**, 359–369 (2007)
118. Lange, A., Luca, S., Baldus, M.: Structure constraints from protein-mediated rare-spin correlation spectroscopy in rotating solids. J. Am. Chem. Soc. **124**, 9704–9705 (2002)
119. Wang, S., Munro, R.A., Kim, S.Y., Jung, K.-H., Brown, L.S., Ladizhansky, V.: Paramagnetic relaxation enhancement reveals oligomerization interface of a membrane protein. J. Am. Chem. Soc. **134**, 16995–16998 (2012)